Identifying in-silico how microstructural changes in cellular fruit affect the drying kinetics

Kevin Prawiranto [a,b], Jan Carmeliet [b], Thijs Defraeye [a *]

[a] *Empa, Swiss Federal Laboratories for Materials Science and Technology, Laboratory for Biomimetic Membranes and Textiles, Lerchenfeldstrasse 5, CH-9014 St. Gallen, Switzerland*

[b] *Chair of Building Physics, Swiss Federal Institute of Technology Zurich (ETHZ), Stefano-Franscini-Platz 5, 8093 Zurich, Switzerland*

Abstract

Convective drying of fruits leads to microstructural changes within the material as a result of moisture removal. In this study, an upscaling approach is developed to understand and identify the relation between the drying kinetics and the resulting microstructural changes of apple fruit, including shrinkage of cells without membrane breakage (free shrinkage) and with membrane breakage (lysis). First, the effective permeability is computed from a microscale model as a function of the water potential. Both temperature dependency and microstructural changes during drying are modeled. The microscale simulation shows that lysis, which can be induced using various pretreatment processes, enhances the tissue permeability up to four times compared to the free shrinkage of the cells. Second, via upscaling, macroscale modeling is used to quantify the impact of these microstructural changes in the fruit drying kinetics. We identify the formation of a barrier layer for water transport during drying, with much lower permeability, at the tissue surface. The permeability of this layer strongly depends on the dehydration mechanism. We also quantified how inducing lysis or modifying the drying conditions, such as airspeed and relative humidity, can accelerate the drying rate. We found that inducing lysis is more effective in reducing the drying rate (up to 26%) than increasing the airspeed from 1 to 5 m/s or decreasing the relative humidity from 30% to 10%. This study quantified the need for including cellular dehydration mechanisms in understanding fruit drying processes and provided insight at a spatial resolution that experiments almost cannot reach.

Keywords: multiscale, drying, fruit cell, deformation, lysis, apple

* Corresponding author.
Address: Laboratory for Biomimetic Membranes and Textiles, Empa, Lerchenfeldstrasse 5, CH-9014 St. Gallen, Switzerland
Email: thijs.defraeye@empa.ch
Telephone: + 41 58 765 4790
Fax: +41 58 765 6909

1 Introduction

Cellular foods such as fruits and vegetables contain typically 60% to 90% water (ASHRAE, 2006). They are highly perishable since the high water activity promotes enzymatic and microbial activity. Drying is a commonly used method to reduce water activity in food products. As such, the product shelf life can be significantly prolonged, thus reducing food waste (Caccavale, De Bonis and Ruocco, 2016). The most popular drying method is convective drying with hot air (Bazyma *et al.*, 2006; Soysal *et al.*, 2009; Castro, Mayorga and Moreno, 2018). During convective drying, water is transported from the material interior to the air-material interface and then from this surface to the drying air. Two barriers influence moisture transport and the corresponding drying kinetics. The first is the external resistance from the surface to the environment, so the boundary layer, as a result of the airflow at the fruit surface by the drying air (Rodríguez *et al.*, 2018). The second is the internal resistance of the tissue that depends on the moisture permeability of the tissue and the temperature.

In fruits and vegetables, water is located mainly inside the cell's protoplast (Molz, 1976). The protoplast is surrounded by the cell membrane and the cell wall. The water migration out of the cell leads to turgor pressure loss and microstructural changes such as cell shrinkage, cell membrane detachment (plasmolysis) or cell membrane breakage (lysis) (Mayor & Sereno 2004; Seguí et al. 2010; Lang et al. 2014). In convective drying of fruit, pretreatments such as thermal blanching (Yoshida *et al.*, 2014; Orikasa *et al.*, 2018), ultrasound (Schössler, Jäger and Knorr, 2012; Tao and Sun, 2015) and pulsed electric field (PEF) treatments (Lebovka, Shynkaryk and Vorobiev, 2007; Liu *et al.*, 2016) are often carried out before the drying process. These processes can improve the drying rate by improving the cell membrane permeabilization or by destroying of the microstructure (Ando *et al.*, 2016; Deng *et al.*, 2017). A mechanistic modeling study by (Prawiranto *et al.*, 2018) shows that microstructural changes directly affect the permeability and sorption isotherm of the tissue. Therefore, in the drying process design or optimization, the change in microstructure should be taken into consideration. Analyzing the impact of these microstructural changes on the drying kinetics is however challenging as it occurs at the microscale scale, by which it is still largely unknown. Apart from experiments, mechanistic modeling could provide a solution here, especially at the lower scales.

Mechanistic modeling has been developed as a tool to understand, design, and control food drying processes in-silico. Two spatial scales are commonly considered: the macroscale and the microscale (10^{-6}–10^{-4} m). At the macroscale, the food material is modeled as a continuum, homogeneous material in which heat and mass transport are solved. Modeling at this scale is used extensively, for example in (Janjai *et al.*, 2008; Aregawi *et al.*, 2013; Barati and Esfahani, 2013; da Silva, e Silva and Gomes, 2013; Shahari and Hibberd, 2014; Gulati and Datta, 2015; Defraeye, 2017; Lemus-Mondaca *et al.*, 2017; Castro, Mayorga and Moreno, 2019; Onwude *et al.*, 2019). The moisture transport is modeled by relying on effective properties such as effective moisture diffusivity (D_{eff}) or permeability (K_{eff}). *These* are macroscopic parameters that lump together the moisture transport mechanisms within the fruit and are keys for the accuracy of mechanistic modeling. Most macroscale models in food dehydration assume a constant value of D_{eff} throughout the drying process, although the moisture content is drastically changing during drying (Rahman *et al.*, 2016). These parameters are mostly obtained experimentally. They can be derived from the drying curves (Velić *et al.*, 2004; Kaya, Aydin and Demirtaş, 2007; Vega-Galvez *et al.*, 2012), from the sample moisture distribution (Nguyen *et al.*, 2003), or by using imaging techniques (Léonard *et al.*, 2008). These empirical properties do often give a good agreement with the experimental drying characteristics (e.g., drying rate). However, they offer limited insights into the phenomena happening at the microscale, for example, cellular shrinkage and deformation. These properties also lump all temporal changes of the diffusivity or permeability into one average value. As such, the used values of D_{eff} or K_{eff} are typically only valid for the specific drying condition they are determined for.

Microscale modeling, on the other hand, is able to explicitly include the complex changes in microstructure and the different cellular components that have different transport properties. Some examples are 2D models that use the Finite Element Method (FEM) to calculate gas diffusivity in pear (Ho *et al.*, 2013) and moisture permeability of pear (Fanta *et al.*, 2013) and apple (Aregawi *et al.*, 2014). These works all looked at a high water activity range, which is typical for fresh fruits. A meshless 2D model has also been developed to study the micromechanics that governs microstructural changes of apple cells during dehydration (H. C P Karunasena *et al.*, 2014; H.C.P. Karunasena *et al.*, 2014; Karunasena *et al.*, 2015). These studies coupled the Smoothed Particle Hydrodynamics (SPH) modeling of protoplast with Discrete Element Method (DEM) modeling of cell wall. A microscale 3D model was used to derive the moisture permeability and sorption isotherm of apple tissue undergoing complete dehydration (Prawiranto *et al.*, 2018). The starting point was cells in fully turgid conditions, which dehydrated according to three different modes: free shrinkage, plasmolysis, and lysis. Here, the effect of the microstructural changes on the effective moisture transport properties has been identified. Nevertheless, the resulting impact on the macroscopic fruit drying kinetics was not studied yet. For this purpose, an upscaling approach can be used (Ho

et al., 2013) to link the macroscale and microscale. By transferring the effective transport properties obtained from the microscale to a macroscale model, the macroscopic modeling is able to calculate the effect of temporal changes in the tissue microstructure on the drying rate and moisture content distribution. The approach has not yet been done so far to analyze the fruit drying process until complete dehydration, to the best knowledge of the authors. However, in food science, multiscale approaches have been used before to study the gas transport in pear fruit (Ho *et al.*, 2011), apple fruit dehydration during long term storage of fresh fruit (Aregawi *et al.*, 2014), and fruit deformation during drying (Wijerathne *et al.*, 2019). Those drying studies, however, show limited moisture removal and overlook the complete dehydration.

By using such an upscaling approach, this study aims to quantify the impact of dehydration-induced microstructural changes on the macroscopic drying process of soft cellular food, in this case, apple fruit, until complete dehydration. Such knowledge is not only essential for having better understanding and control over the drying process, but also in optimizing appropriate pretreatments that could improve the drying process. We analyzed the drying kinetics for different cellular dehydration mechanisms were considered, namely free shrinkage and lysis. Free shrinkage implies that the cells only shrink during drying, while lysis involves the breakage of cell membrane during dehydration. In addition, we also quantified how different drying rates induce differences in the microstructural changes within the tissue and how such changes influence the drying rate and moisture distribution of the fruit tissue.

2 Materials and Methods

The work is divided into two parts, i.e., microscale (cellular scale) and the macroscale (fruit sample) modeling. The microscale model (Section 2.1) is used to determine the impact of microstructural changes and temperature on the effective permeability and sorption isotherm. By upscaling, these properties are used in the macroscale model (Section 2.2) to solve the heat and mass transport together with the dehydration-driven deformation.

2.1 Modeling at the cellular scale

2.1.1 Obtaining the cellular geometry

The cellular geometry of the fruit tissue used in the microscale modeling was obtained by X-ray micro-computed tomography (CT). A cylindrical apple sample with a diameter of 8 mm and a height of 15 mm was extracted from the inner cortex using a cork borer. The experiments were done at the Empa Center for X-ray Analytics (Switzerland). The X-ray micro-CT setup consisted of an X-ray tube (XT9160-TXD, Viscom, Hannover, Germany), a high-precision rotation table (UPR-160F AIR, Micos, Dübendorf, Switzerland) and a flat panel detector (XRD-1621-CN3ES, Perkin Elmer, Waltham, USA). The system used a power source of 20 W at 70 kV and 285 µA. The center of the sample was at a distance of 590 mm from the scintillator. The sample was rotated over 360° in angular steps of 0.5°. Seven hundred and twenty-one images were generated for one tomogram dataset. Each image had 1800 × 1800 pixels and a pixel size of 8.85 × 8.85 µm^2.

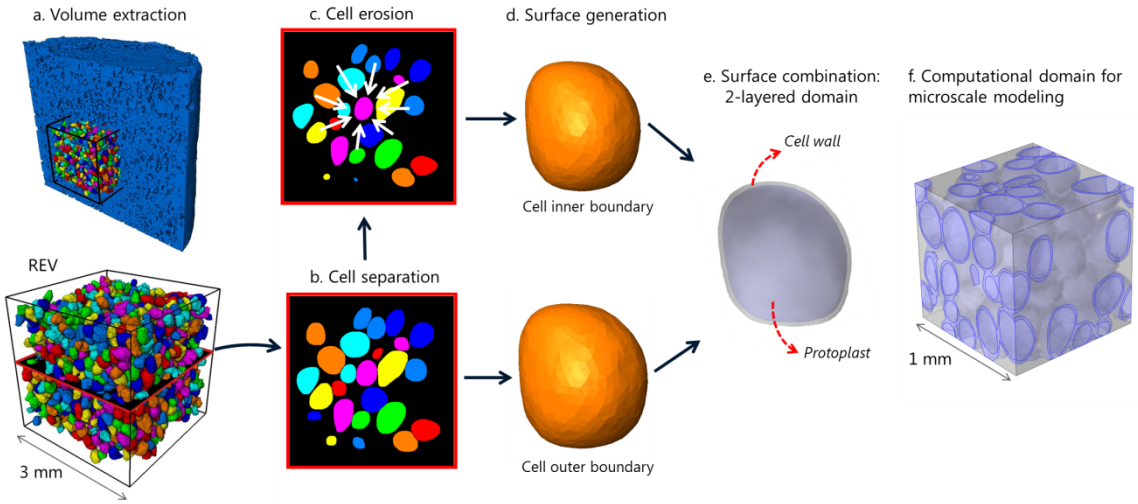

Figure 1. Illustration of the image processing steps carried out to obtain the computational domain for the microscale modeling. (a) After image filtering and cell segmentation, a Representation Elementary Volume (REV) is extracted from the tissue. (b) The cells in the REV are separated into individual cells with a watershed algorithm. (c) To create a two-layered computational domain within the cells (in order to account for the cell wall), the separated cells are eroded. (d) The cell outer and inner boundaries are created out of the separated cells and eroded cells, respectively. (e) The surfaces are then combined and converted into a solid domain to form the cell wall and protoplast domains. (f) An example of the generated computational domain is shown for a REV with an edge length of 1 mm.

The raw images of the X-ray micro-CT are reconstructed using Octopus Reconstruction software version 8.9.3 (XRE, Gent, Belgium). The post-processing steps of the reconstructed images are adopted from (Prawiranto *et al.*, 2019) and performed using the commercial software Avizo (Edition 9.5, Thermo Fisher Scientific, Waltham, USA). As a first step, the noise in the raw X-ray images is removed by using an anisotropic diffusion filter to preserve the details of the edges (Tschumperlé & Deriche 2005). The cell material is segmented out from the images by applying a global threshold. A cuboid Representative Elementary Volume (REV) is extracted from the sample (Figure 1a) with a specific size (explained in detail in Section 2.1.5). The cell material in the REV was separated into individual cells (Figure 1b) by a watershed algorithm (Baldwin *et al.*, 1996). For the microscale modeling, two domains need to be created within the cell material to model the protoplast and the cell wall separately. To do so, the separated cells are eroded to create a wall thickness (Figure 1c). Delaunay triangulation (Lee and Schachter, 1980) is used to convert the separated cells (Figure 1b) and eroded cells (Figure 1c) into

surfaces. The surfaces are imported into COMSOL Multiphysics (COMSOL AB, Stockholm, Sweden) as two STL files and converted into separate solid domains for the cell wall and protoplast (Figure 1e). By a Boolean operation, these domains are combined within a cubic domain that has the corresponding REV edge length. Thereby, an additional domain for the extracellular air (space in between the cells) is generated. The cellular compartments that intersected with the border of the cube were cut (Figure 1f). The cutting is done to avoid cell removal at the boundary and changes in volume ratio of cellular compartments that could impact the resulting permeability calculation (explained in Section 2.1.5).

2.1.2 Moisture transport model at the microscale

The microscale modeling approach of Prawiranto et al. (2018) is used. Only the key details are presented here. The model is adjusted to take into account the influence of temperature on the moisture transport properties of the cellular components, namely protoplast, cell wall and intercellular space. In a steady-state condition, the following mass conservation equation is solved for each of the cellular components:

$$\nabla \cdot \left(K_i \nabla \psi_i \right) = 0 \tag{1}$$

where K_i is the water permeability of the cellular component i [s], and ψ_i is the water potential [Pa]. Modifications to the permeability formulation are made for each cellular component to take into account the impact of temperature T on the diffusivity of the cellular component D_i. For the protoplast, the water permeability K_c is:

$$K_c = D_c \left(\frac{\rho_{dm,c} C_{\psi,c}}{1 + x_c} \right) \tag{2}$$

where $\rho_{dm,c}$ is the dry matter density [kg m^{-3}], D_c is the water diffusivity [m^2 s^{-1}], $C_{\psi,c}$ is the water capacity [Pa^{-1}], and x_c is the dry basis water content [kg kg^{-1}] of the protoplast. D_c is calculated based on the water self-diffusion coefficient (Holz, Heil, Stefan and Sacco, 2000):

$$D_c = D_{c,0} \left(\frac{T}{T_s} - 1 \right)^{\gamma} \tag{3}$$

where $D_{c,0}$, T_s, and γ are model parameters. The water capacity of the protoplast $C_{\psi,c}$ depends on the underlying microstructural changes. When the cell is in a turgid condition, the correlation below applies (Prawiranto *et al.*, 2018):

$$C_{w,c} = \frac{\partial x_c}{\partial \psi_s} = 1.14 \times 10^{-12} \psi_c + 4.53 \times 10^{-6} \tag{4}$$

When the cell undergoes free shrinkage, $C_{\psi,c}$ is a function of the density of water ρ_w, the molar mass of solutes in the protoplast M_s, osmotic potential ψ_s, the gas constant R, and the temperature T.

$$C_{\psi,c} = \frac{\partial x_c}{\partial \psi_s} = \frac{\rho_w}{{\psi_s}^2 M_s} RT \tag{5}$$

By considering the protoplast as a dilute solution with a solute concentration of less than one molar (Yamaki, 1984), the osmotic potential can be calculated from the Van't Hoff approximation (Fanta *et al.*, 2013):

$$\psi_s = -\frac{\rho_w}{x_c M_s} RT \tag{6}$$

For the cell wall, the permeability K_w is defined as:

$$K_w = \rho_{dm,w} D_w C_{\psi,w} \tag{7}$$

where $\rho_{dm,w}$ is the dry matter density [kg m^{-3}], D_w is the water diffusivity [m^2 s^{-1}], and $C_{\psi,w}$ is the water capacity [Pa^{-1}] of the cell wall. D_w is derived using the Arrhenius law from the diffusivity values of an artificial cell wall at T = 3 and 25 °C (Fanta *et al.*, 2012):

$$D_w = D_{w,0} \exp\left(\frac{-a}{RT} \right) \tag{8}$$

where $D_{w,0}$, and a are model parameters. In the intercellular air space, the water permeability is given by:

$$K_a = \rho_{dm,a} D_a C_{\psi,a} \tag{9}$$

where $\rho_{dm,a}$ is the dry matter density [kg m^{-3}], D_a is the water diffusivity [m^2 s^{-1}], and $C_{\psi,a}$ is the water capacity [Pa^{-1}] of the air. D_a is empirically determined by (Marrero and Mason, 1972) as:

$$D_a = D_{a,0}\left(\frac{T^g}{P}\right) \tag{10}$$

where $D_{a,0}$ and g are model parameters, and P is the pressure (1 atm). The cell membrane that encapsulates the cell protoplast is not explicitly discretized in the model. Instead, it is modeled as a thin membrane by including an internal resistance between the protoplast and the cell wall. As such, the water flux J at their interface is defined as (Nobel, 2009):

$$J = \frac{\rho_w P_m V_w}{RT}\left(\psi_c - \psi_a\right) \tag{11}$$

where ρ_w is the water density [kg m^{-3}], and P_m is the membrane permeability coefficient. The relevant material properties and model parameters are specified in Table 2.

2.1.3 The dehydration-driven deformation at the microscale

The following mechanical equilibrium is used to calculate the cell deformation, assuming no body and surface forces (Bonet and Wood, 2008):

$$\nabla \cdot \left(\mathbf{S} \cdot \mathbf{F}^T\right) = 0 \tag{12}$$

where $\mathbf{S}$ is the second Piola–Kirchhoff stress tensor and $\mathbf{F}^T$ is the transpose of the elastic deformation gradient tensor $\mathbf{F}$. The second Piola–Kirchhoff stress tensor is defined as a function of the strain energy density W_s:

$$\mathbf{S} = \frac{\partial W_s}{\partial \mathbf{E}} \tag{13}$$

where $\mathbf{E}$ is the elastic Green–Lagrange strain tensor that is described as:

$$\mathbf{E} = \frac{1}{2}\left(\mathbf{F}^{\mathrm{T}}\mathbf{F} - 1\right) \tag{14}$$

A neo-Hookean constitutive model is chosen to account for the large material deformation occurring due to moisture loss (Gulati and Datta, 2015) and the deformation is assumed to be isotropic. Here, the strain energy density function is:

$$W_s = \frac{K}{2}\left(J_{el} - 1\right)^2 - \frac{G}{2}\left(\overline{I_1} - 3\right) \tag{15}$$

where K is the bulk modulus [Pa], J_{el} is the elastic Jacobian, G is the shear modulus [Pa], and I_1 is the first invariant of the elastic right Cauchy–Green tensor. K and G are determined from the elastic Young's modulus E and Poisson's ratio v:

$$K = \frac{E}{3\left(1 + 2v\right)} \tag{16}$$

$$G = \frac{E}{2\left(1 + v\right)} \tag{17}$$

The elastic Jacobian J_{el} is obtained as the ratio of total Jacobian, J, and volume changes due to moisture effects, J_m:

$$J_m = \frac{V_t}{V_0} = \left(1 + \beta\left(x_{t,i} - x_{0,i}\right)\right)^3 \tag{18}$$

where V_t is the volume at time t [m^{-3}], V_0 is the initial volume [m^{-3}], $x_{t,i}$ is the dry matter water content at time t of component i, $x_{0,i}$ is the initial dry basis water content component i, and β is the volumetric shrinkage coefficient. During drying, V_t is assumed to be equal to the volume of the water removed from the tissue. It is formulated as follows:

$$\frac{V_t}{V_0} = 1 - \frac{\rho_{s,i}}{\rho_l}\left(x_{0,i} - x_{t,i}\right) \tag{19}$$

where $\rho_{s,i}$ is the dry matter density of component i [kg m^{-3}], and ρ_s is the liquid water density [kg m^{-3}]. The shrinkage coefficient is calculated as:

$$\beta = \frac{\left(1 - \frac{\rho_s}{\rho_l}\left(x_{0,i} - x_t\right)\right)^{1/3} - 1}{x_{t,i} - x_{0,i}} \tag{20}$$

The deformation model is applied to the protoplast and cell wall. The air domain is modeled with a moving mesh with boundary deformations that follows the deformation of cell wall and protoplast. The material properties are presented in Table 2.

Table 2. Material properties and model parameters used for the microscale model.

Material properties	Value	Unit	Reference
Diffusivity parameters			
$D_{c,0}$	1.64×10^{-8}	$m^2\ s^{-1}$	(Holz, Heil, Stefan and Sacco, 2000)
T_s	215.05	K	(Holz, Heil, Stefan and Sacco, 2000)
γ	2.063	-	(Holz, Heil, Stefan and Sacco, 2000)
$D_{w,0}$	1.41×10^{-9}	$m^2\ s^{-1}$	Calculated (Eq. 1.8)
a	1.06×10^{5}	$kg\ m^2\ s^{-2}\ mol^{-1}$	Calculated (Eq. 1.8)
$D_{a,0}$	1.87×10^{-10}	$m^2\ s^{-1}$	(Marrero and Mason, 1972)
g	2.072		(Marrero and Mason, 1972)
Dry matter density			
Protoplast, $\rho_{dm,c}$	120	$kg\ m^{-3}$	(Constenla, Lozano and Crapiste, 1989)
Cell wall, $\rho_{dm,w}$	58.035	$kg\ m^{-3}$	(Fanta *et al.*, 2012)
Intercellular air space, $\rho_{dm,a}$	1.184	$kg\ m^{-3}$	(Coulson *et al.*, 1999)
Water capacity of air, $C_{\psi,a}$	1.3×10^{-10}	$1\ Pa^{-1}$	(Coulson *et al.*, 1999)
Membrane permeability coefficient, P_m	2×10^{-5}	$m\ s^{-1}$	(Ferrando and Spiess, 2001; Moshelion, Moran and Chaumont, 2004)
Molar mass of solutes, M_s	0.203	$kg\ mol^{-1}$	(Tortoe, Orchard and Beezer, 2008)
Molar volume of water, V_w	1.8×10^{-5}	$m^3\ mol^{-1}$	
Zero turgid point ($a_{w,\ turgid}$)	0.97	-	(Prawiranto *et al.*, 2018)
Poisson ratio, ν	0.49	-	(Naiqian and Pitts, 1999)
Bulk modulus, K	5.8 x107	Pa	(Naiqian and Pitts, 1999)

2.1.4 Boundary conditions

For a simulation of the transport properties at a certain water activity, water activities which are 0.05% higher (ψ_1) and 0.05% lower (ψ_2) than the target water activity are imposed at the top and bottom boundaries (Dirichlet boundary conditions). Zero flux boundary conditions are set on the lateral boundaries (Figure 2). The effective permeability, K_{eff} [s] is calculated as:

$$K_{eff}(\psi) = -J\frac{L}{(\psi_1 - \psi_2)} \tag{20}$$

where J is the total steady-state flux over the entire cellular structure [$kg\ m^{-2}\ s^{-1}$], $(\psi_1 - \psi_2)$ is the applied water potential difference over the top and bottom boundaries [Pa], and L is the thickness of the simulated cellular structure. The tissue water permeability K_{eff} can be related to the effective water diffusivity D_{eff} [$m^2\ s^{-1}$] in the tissue via the effective capacity C_{eff} [Pa^{-1}]:

$$D_{eff}(\psi) = \frac{K_{eff}}{\rho_{dm} C_{eff}} \tag{21}$$

The effective capacity can be derived from the sorption isotherm, which is the relation between water content x and water activity ψ, such that:

$$C_{eff} = \frac{\partial x}{\partial \psi} \tag{22}$$

The effective permeability and corresponding diffusivity lump all possible transport mechanisms of liquid water and water vapor in the cellular structure. The tissue sorption isotherm is derived from the microscale simulations by averaging the water content of the three cellular components (protoplast, cell wall, and intercellular air space) at a given water activity according to their volume fractions. For deformation modeling, free deformation is applied to all domains and the top boundary. Zero normal displacements are set for the bottom and lateral boundaries.

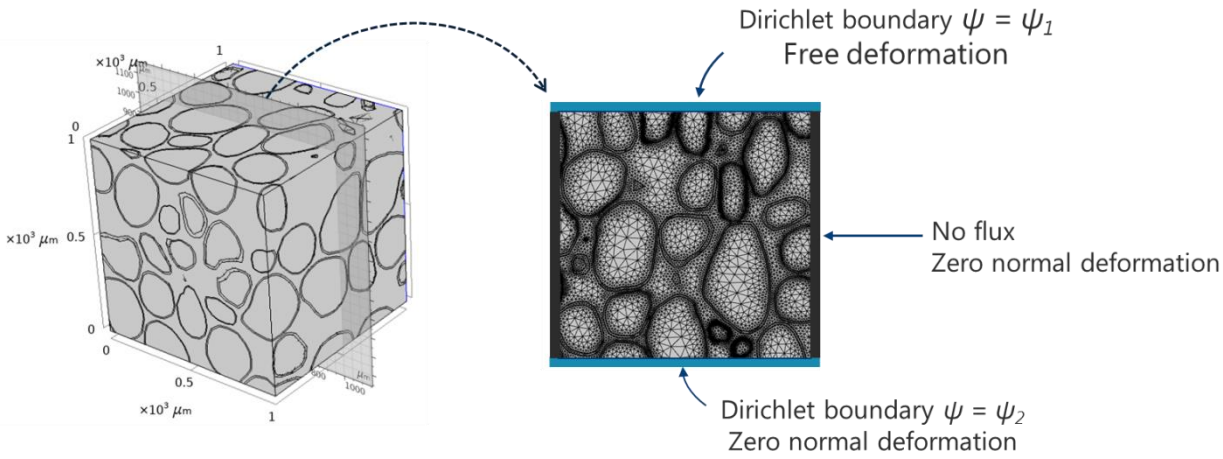

Figure 2. Boundary conditions and meshing in the microscale model.

2.1.5 Defining the Representative Elementary Volume (REV)

An analysis of the required size of a Representative Elementary Volume (REV) is done to see how large this should be. The REV should be large enough to enable effective transport properties to be calculated for the considered microstructure, but small enough to reduce the computational cost (Gitman, Askes, & Sluys, 2007; Pellegrino, Galvanetto, & Schrefler, 1999). In the REV analysis, first we compare the air space volume fraction (porosity) for different sizes of REV, since the fraction of air space to cellular components within a tissue influences the effective permeability (Prawiranto *et al.*, 2018). From the cylindrical tissue described in Section 2.1.1, which has a diameter of 8 mm and a height of 8 cm, a cuboid REV is extracted with an edge length of 6 mm. The porosity of this cuboid is calculated. In addition, out of this 6 mm cuboid, eight cuboids with an edge length of 3 mm and 20 randomly selected cuboids with an edge length of 2 mm, 1 mm, 0.5 mm, 0.25 mm, and 0.1 mm are extracted (Figure 3). The porosity of all cuboid samples is computed, and the results are presented in Table 3. When the REV becomes smaller, the standard deviation of the porosity increases. For a REV size of 0.5 mm and above, the mean of porosity is close to the one of the 6 mm REV (27%). An increase in standard deviation is observed when the REV edge length decreases from 0.5 mm to 0.25 mm. Here, 250 micron is close to the average diameter of a single cell size that was found in the range of 170 to 220 µm (Herremans *et al.*, 2015; Prawiranto *et al.*, 2019), which is thereby definitely too small for a REV. The 0.1 mm REV is smaller than average cell diameter. Thereby, it may contain only a pore or a cell. From this REV analysis, the 0.5 mm cuboids are the smallest possible REVs that can be used.

Table 3. Porosity analysis of different REV sizes

Dimension (mm^3)	Number of samples	Mean (%)	Standard deviation (%)
6 x 6 x 6	1	27.0	-
3 x 3 x 3	8	27.1	2.3
2 x 2 x 2	20	27.5	3.6
1 x 1 x 1	20	28. 2	3.7
0.5 x 0.5 x 0.5	20	28.0	4.9
0.25 x 0.25 x 0.25	20	24.9	10.6
0.1 x 0.1 x 0.1	20	21.3	27.9

In addition to the porosity analysis, we also calculate the effective permeability of different sizes of REV with an edge length of 3 mm, 2 mm, 1 mm, 0.5 mm, and a unit cell (Table 4). The details of the calculation is presented in Supplementary Material A. Note that the samples each have a slightly different volume fraction of the cellular components. Table 4 shows that the calculated K_{eff} fluctuates within 13% between samples. This number is considered small and acceptable considering the large variability of K_{eff} (and D_{eff}), up to several orders of magnitude, which is reported in the literature (Defraeye and Verboven, 2016). With respect to the porosity and permeability analysis, we conclude that it is sufficient to have a REV size of 0.5 mm or larger. To be on the safe side, the microscale simulations were performed for a 1 mm REV.

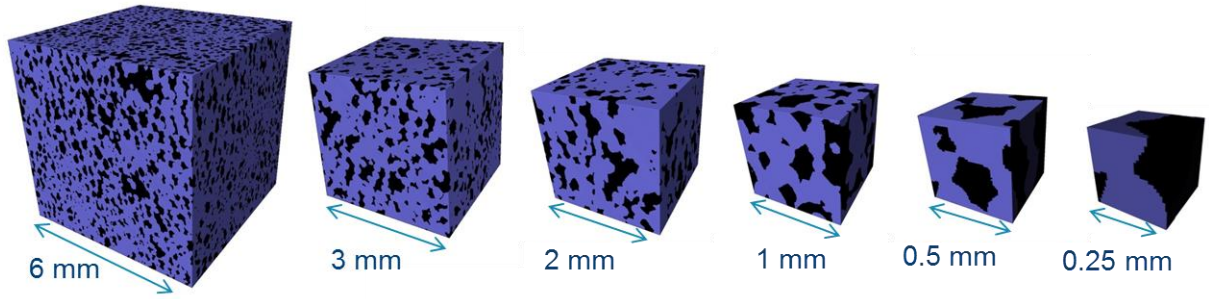

Figure 3. The porosity of different REV sizes is evaluated in the REV analysis. Porosity is the ratio of air space volume (black color) to the total volume of the REV. Figures are not to scale.

Table 4. Calculated K_{eff} at a_w = 0.98 for different REV sizes

Sample	Dimension (mm^3)	Pore volume (%)	Protoplast volume (%)	Cell wall volume (%)	K_{eff} [s]	ΔK_{eff} (%)
1	3 x 3 x 3 mm^3	27	40	29	9.69 x 10^{-14}	0
2	2 x 2 x 2 mm^3	28	45	27	1.11 x 10^{-13}	-12.7
3	1 x 1 x 1 mm^3	30	46	24	1.03 x 10^{-13}	-5.92
4	0.5 x 0.5 x 0.5 mm^3	39	41	20	8.58 x 10^{-14}	12.94
5	Cuboctahedral single cell (Prawiranto *et al.*, 2018)	32	42	26	1.08 x 10^{-13}	-10.36

2.2 Modeling at the macroscale

2.2.1 Heat and moisture transport

A validated macroscale model (T. Defraeye and Verboven 2016) is used to calculate the heat and water transfer in fruit tissue during drying. Here, the water transport is driven by the water potential differences. The following conservation equations for moisture and energy are solved simultaneously:

$$\frac{\partial w_m}{\partial \psi}\frac{\partial \psi}{\partial t} + \nabla \cdot \left(K_{eff} \nabla \psi \right) = 0 \tag{23}$$

$$\left(c_{p,s} w_s + c_{p,l} w_m \right) \frac{\partial T}{\partial t} + \nabla \cdot \left(-\lambda_{PM} \nabla T \right) = 0 \tag{24}$$

where ψ is water potential [Pa], T is temperature [K], w_s is dry matter density [kg m^{-3}], w_m is the moisture content of the tissue [kg m^{-3}], K_{eff} is the moisture permeability of the tissue that is taken from the microscale modeling, h_l is the enthalpy of liquid water [J kg^{-1}], λ_{PM} is the thermal conductivity of the tissue [W m^{-1} K^{-1}], and $c_{p,s}$ and $c_{p,l}$ are the specific heat capacities of dry matter and liquid water [J kg^{-1} K^{-1}], respectively. ψ is related to the water activity a_w by:

$$\psi = \rho_l R_v T \ln\left(a_w \right) \tag{25}$$

The following boundary conditions are specified at the air-tissue interface, implying the continuity of moisture and heat flux:

$$\mathbf{n} \cdot \left(K_m \nabla \psi \right) = g_m = \mathrm{CMTC}\left(p_{v,m} - p_{v,ref} \right) \tag{26}$$

$$\mathbf{n} \cdot \left(-h_l K_m \nabla \psi - \lambda_{PM} \nabla T \right) = g_T = \left(\mathrm{CHTC}\left(T_w - T_{ref} \right) - h_v g_m \right) \tag{27}$$

where g_m [kg m^{-2} s^{-1}] and g_T [J m^{-2} s^{-1}] are the mass and heat fluxes at the interface, **n** is the unit vector normal to the interface, CMTC is the convective mass transfer coefficient [s m^{-1}], CHTC is the convective heat transfer coefficient [W m^{-2} K^{-1}], $p_{v,w}$ and $p_{v,ref}$ are the vapor pressures at the interface and of the ambient air [Pa], T_w and T_{ref} are the temperatures at the interface and of the ambient air [K], and h_v and h_l are the enthalpies of water vapor and liquid water [J kg^{-1}], respectively. h_v and h_l are calculated as:

$$h_l = c_{p,l}\left(T - T_{ref,0} \right) \tag{28}$$

$$h_v = c_{p,v}\left(T - T_{ref,0} \right) + L_v \tag{29}$$

where L_v is the latent heat of water [J kg^{-1}], and $T_{ref,0}$ is the reference temperature (273.15 K).

2.2.2 Deformation

The same Neo-Hokeean hyperelastic model, as explained in Section 2.1.3, is applied to model the tissue deformation due to dehydration. The elastic properties of the tissue are presented in Table 5.

Table 5. Material properties for the macroscale modeling

Material property	Value	Unit	Reference
Thermal conductivity of fruit tissue	0.418	W m^{-1} K^{-1}	(ASHRAE, 2006)
Specific heat capacity of dry matter of fruit	1634	J kg^{-1} K^{-1}	(ASHRAE, 2006)
Specific heat capacity of liquid water	4182	J kg^{-1} K^{-1}	(Maloney, 2007)
Specific heat capacity of water vapor	1880	J kg^{-1} K^{-1}	(Maloney, 2007)
Dry matter density	130	kg m^{-3}	(Defraeye and Verboven, 2016)
Density of liquid water	1000	kg m^{-3}	(Maloney, 2007)
Latent heat of water	2.5×10^6	J kg^{-1}	(Maloney, 2007)
Specific gas constant of water vapor	461.52	J kg^{-1} K^{-1}	(Maloney, 2007)
Poisson ratio	0.499	-	(Wang, Wang and Thomas, 2004)
Elastic modulus	5×10^5	Pa	(Wang, Wang and Thomas, 2004)

2.2.3 Geometry and boundary conditions

The accuracy of the multiscale modeling is assessed by comparing the results of macroscale simulation with experimental results of (Defraeye and Verboven, 2016). The details of the boundary conditions and modeling results can be found **Supplementary Material B**. To study the relationship between the microstructural changes and drying rate at the macroscale, a cuboid with an edge length of 20 mm (Figure 4a) is used to represent the tissue sample. Due to symmetry, only one-eighth of the geometry is modeled (Figure 4b). Zero-flux boundary conditions and zero normal displacements are imposed on the symmetrical planes. For model simplification, the exposed sides of the cubes are assumed to have a uniform CHTC and CMTC, and are free to deform (unconstrained). CHTC is calculated based on the assumption of turbulent flow around a square cylinder in a crossflow (Igarashi, 1985; Kapitz *et al.*, 2018).

$$\mathrm{CHTC} = \frac{0.14\,\mathrm{Re}^{0.66}\,\mathrm{Pr}^{0.33}\,k_a}{l(t)} \tag{30}$$

where Re is the Reynolds number [-], Pr is the Prandtl number [-], k_a is the thermal conductivity of air [W m^{-1} K^{-1}], and $l(t)$ is the length of the object at time t [m]. The CMTC is calculated from CHTC by using the Chilton-Colburn analogy of heat and mass transfer (Chilton and Colburn 1934; Thijs Defraeye, Blocken, and Carmeliet 2012). The analogy applies with certain criteria: 1) the flow field is not influenced by heat and mass transfer (thus valid only for forced convection or low mass transfer rate), 2) only convective heat and mass transfer occur between the material and environment, so no other heat or mass sources including radiation are present, 3) heat and mass transfer are uncoupled, so they do not influence one another, 4) analogous temperature and mass concentration boundary conditions, and 5) the Lewis number equals to one. Although the third and fourth criteria are basically not satisfied in the simulated drying conditions, the use of the analogy is still justified, as it is shown by the study of (T. Defraeye and Verboven 2016). Here, apple drying simulations are done within the range of the drying conditions used in this study (CHTC = 10 – 31 W/m^{2}K, drying temperature = 20 – 60°C, RH = 30%).

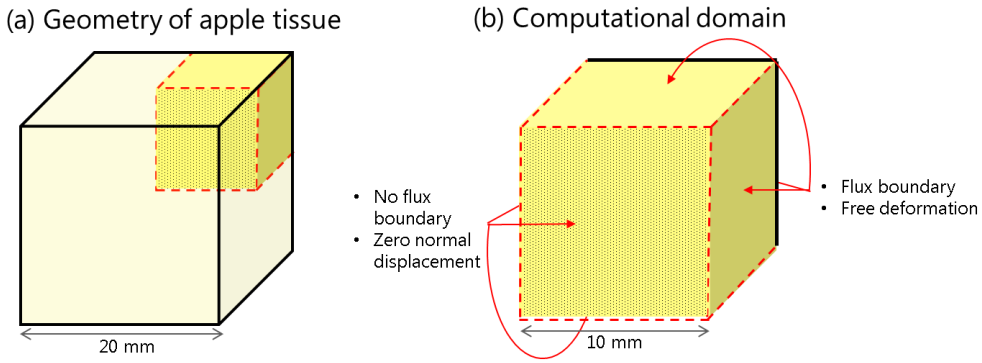

Figure 4. Computational domain of the apple tissue and indication of the boundary conditions used in the macroscale model.

2.2.4 Base case

A base case is simulated for the cells in the tissue that undergo free shrinkage during drying. The effective permeability and water capacity are taken from the values as obtained from the microscale modeling explained in Section 2.1. The initial conditions of the base case are specified in Table 6.

Table 6. Initial and boundary conditions of the base case

Boundary and initial conditions	Value	Unit
Initial tissue temperature	23	°C
Initial tissue dry basis moisture content	5.5	kg kg_{dm}^{-1}
Ambient air temperature	23	°C
Ambient relative humidity	30	%
Airspeed	1	m/s

2.2.5 Parametric study

2.2.5.1 Variation of microstructural changes

The impacts of microstructural changes on the drying rate are analyzed by comparing the base case model of free shrinkage with three additional scenarios:

(1) Total lysis, the case the cell membrane is entirely permeable as such that there is no resistance for water transport. The effective permeability and water capacity are taken from the microscale modeling of this total lysis case.

(2) Natural lysis, which assumes the cell membrane breaks naturally during drying following the turgor loss at the water activity of 0.97. Note that this choice of water activity threshold when lysis occurs at 0.97 was based on the study of (Prawiranto *et al.*, 2018). Considering there is no study that indicates the exact conditions for lysis to happen, this model is used to demonstrate how natural lysis may take place in reality and will affect the drying rate.

(3) The case where a constant K_{eff} is used with a value of 1.41×10^{-15} s, labeled as Keff_cons, so independent of the moisture content. This is the averaged value of K_{eff} at 25°C, where averaging is performed over a tissue with the fully turgid cells at a water activity of 0.99 to a tissue with very dried cells at a water activity of 0.1 (see the results of microscale modeling in Section 3.1). This can be considered as a benchmark for the previous state of the art, where typically constant coefficients are used.

2.2.5.2 Variation of airspeed and relative humidity

The impact of the induced drying rate on the microstructural changes is analyzed by varying the approach flow's airspeed and relative humidity in the macroscale simulation. The evaluated airspeeds are 0.5, 1, 2.5, and 5 [m s^{-1}], that correspond to CHTC of 11.5, 18.2, 33.4, and 52.7 [W $m^{-2} K^{-1}$], respectively. The evaluated relative humidities are 10%, 20%, 30%, and 40%. Here, only free shrinkage and natural lysis cases are compared. The microstructural changes had been induced in the total lysis case before the drying process, so it is not influenced by the drying rate.

2.3 Numerical simulations

The microscale and macroscale simulations are performed using COMSOL Multiphysics version 5.4. Based on a mesh sensitivity analysis, the microscale (base case) and macroscale domains are meshed into 816'714 tetrahedral and 8'061 tetrahedral elements, respectively. The governing equations of water transport (microscale) and of moisture and heat transport (macroscale) are implemented in the coefficient form PDE interface. The Structural Mechanics, Nonlinear Structural Materials, and Deformed Geometry modules of COMSOL are used to model the structural deformation. A direct MUMPS (MUltifrontal Massively Parallel sparse direct Solver) is adopted to solve the resulting systems of equations. The dependent variables are solved by using segregated solver, in which the heat and water transports are solved first and followed by the deformation. The relative tolerances for convergence are set at 1×10^{-4} for all solved variables, which is found to be small enough to make the solution independent of the tolerance value. The macroscale simulations used an adaptive time-stepping, with a maximal time step of 240 s, as determined from a temporal sensitivity analysis. The simulations take about 7 hours for the microscale and 20 minutes for the macroscale on a 2.50-GHz eight-core Intel Core i7 processor with 32 GB of RAM.

3 Results and Discussion

3.1 Impact of microstructural changes and temperature on effective permeability and diffusivity

To investigate the impact of temperature on the tissue's effective permeability, its impact on the permeability of cellular component is firstly examined by solving Equation 2, 7 and 9. The permeability of all cellular components increases with temperature (Figure 5). The temperature has the largest impact on the cell wall permeability. It increases by four orders of magnitude when drying at 80°C, compared to 10°C. At higher temperature, water molecules have more energy and mobility, which enhances water transport. The increase of permeability with temperature is also observed to a smaller extent in the protoplast and air space.

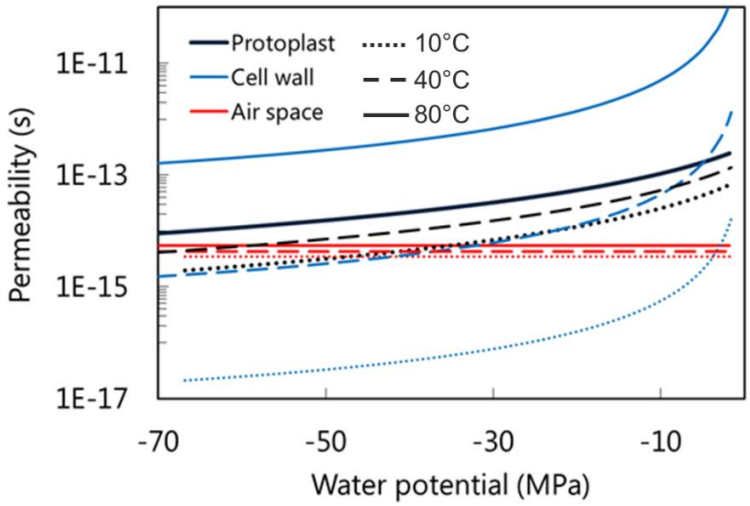

Figure 5. Permeability of cellular components at different temperatures.

The microstructure deforms as the water is removed from the protoplast and cell wall during dehydration. Figure 6a displays examples of water potential profiles of the microstructure in a turgid condition (a_w =0.98) and how the structure deformed when the water activity decreased to 0.7 at 20°C. The height of the deformed structure L is used to calculate the effective permeability as described in Equation (20). Simulations show that the effective permeability of the tissue is observed to increase with temperature (Figure 6b) for both free shrinkage and lysis due to the increase of permeability in the cellular components. The effective permeability can increase by a factor of 40 and 150 in the case of fully turgid (a_w = 0.99) and dried-out cells (a_w = 0.3), respectively, when the temperature rises from 10 to 80 °C. The difference between the effective permeability of free shrinkage and total lysis cases is more pronounced at low temperature. The ratio of the effective permeability of lysis to that of free shrinkage reduces from 4 to 1.1 when the temperature rises from 10 to 80 °C. This phenomenon shows that the main barrier for water transport in free shrinkage, which is provided by the cell membrane, is counteracted by the movement of high-energy water molecules at elevated temperature. The effective diffusivity also increases at a higher temperature as it is directly connected to the effective permeability (Equation 1.22). Tissue with lower water content tends to have higher effective diffusivity due to the lower water capacity. Note that the free shrinkage and lysis cases have a similar water capacity because the equilibrium water content is not influenced by the microstructural changes (Figure 5c). However, the water capacity decreases with temperature, which in line with the findings of (Roman, Urbicain and Rotstein, 1982; Bellagha *et al.*, 2008). The calculated effective diffusivities are within the typical values measured in experiments, which are in the range of 1×10^{-11} to 1×10^{-8} m^2 s^{-1} (Velić et al. 2004; Kaya et al. 2007; Vega-Galvez et al. 2012; Zlatanović et al. 2013). From this microscale simulation, it can be concluded that inducing lysis prior to drying can only be effective in increasing the tissue permeability when the subsequent drying is done at low temperature. At a typical low-temperature drying at 25°C, three times increase of effective permeability is expected when lysis takes place.

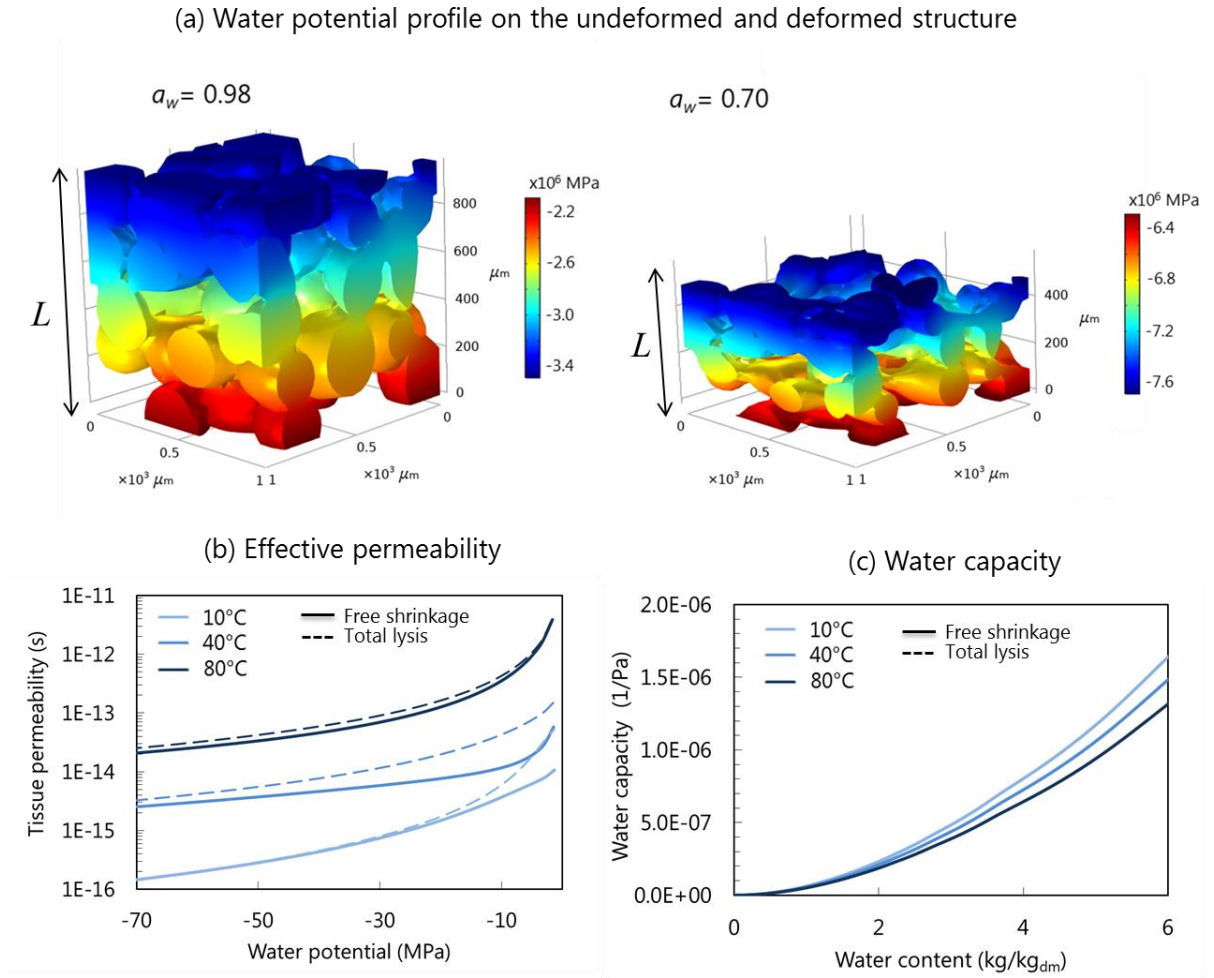

Figure 6. (a) Water potential profile and deformation of the microstructure at a_w =0.98 and 0.70. The simulations are carried out at 20°C. The tissue properties derived from the microscale modeling: (b) effective permeability Keff and (c) water capacity Ceff. The free shrinkage cases are shown by solid lines, while the total lysis cases are shown by dotted lines.

3.2 Impact of microstructural changes on the macroscopic drying kinetics

Comparisons of the macroscale drying kinetics for tissue undergoing different microstructural changes are shown in Figure 7, as well as a model using a constant permeability. The drying rate is calculated based on the total amount of moisture lost per second and per surface area of the fruit, which changes continuously during drying as the tissue shrinks. It is clearly shown in Figure 7a that by inducing membrane breakage prior to the drying process (total lysis through e.g. pretreatment), the drying time to reach a safe water activity of 0.6 is 29% faster than the free shrinkage case. Total lysis maintains high surface water activity during the first seven hours of drying (Figure 7b) that causes a high drying rate during that period (Figure 7c). The drying rate decreases linearly with moisture content (Figure 7d). Natural lysis and free shrinkage have the same drying rate in the first two hours of drying. Natural lysis exhibits a higher drying rate than free shrinkage after this period due to the membrane breakage at a_w = 0.97. However, its drying rate at any level of water content is still significantly lower (30 % lower on average) than in the total lysis case. This suggests that the earlier lysis occurs, the more significant is its impact in accelerating the drying rate. All drying cases display a falling drying rate period, which is a period where the instantaneous drying rate is constantly decreasing.

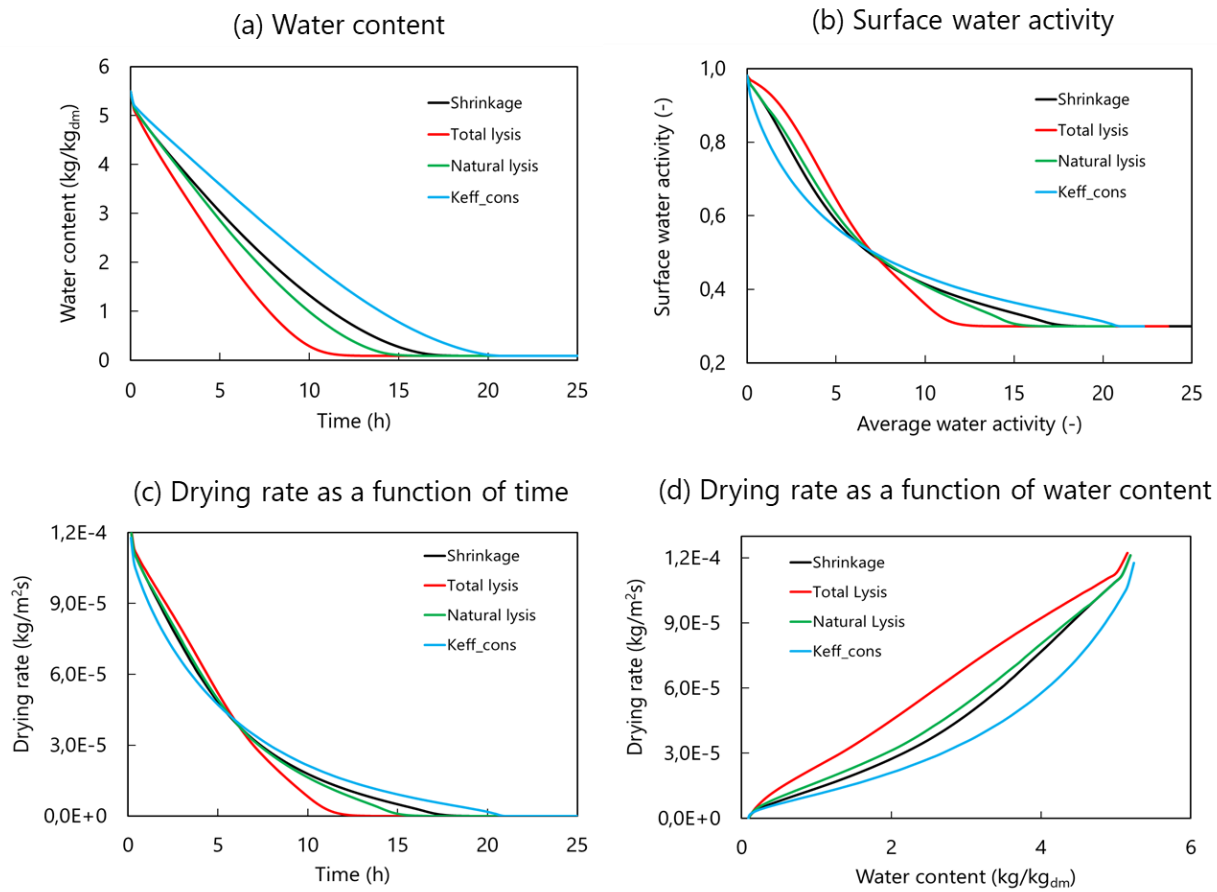

Figure 7. Impact of microstructural changes (free shrinkage, total lysis and natural lysis) on the changes of (a) water content and (b) surface water activity during drying. Drying rate as a function of time (c) and water content (d). The cases are compared to a simulation that is using a constant permeability (K_{eff}_cons) which is typically used in state of the art drying simulations.

The difference in drying rate in the three cases above can be explained in more detail by looking at the spatial profile of water content and permeability across the tissue in Figure 8 and 9. Note that the profiles in each case are obtained at a different point in time when specific average water activity is reached. Each drying case shows a different water content distribution, which can also be linked to the tissue permeability profile in Figure 9. In free shrinkage, the water removal at the surface leads to a thin layer of tissue showing a sharp water gradient making the separation of dry and moist tissue clear (see the area indicated by white arrows in Figure 8a). In this case, a gradual reduction of permeability is shown from the core to the tissue surface (Figure 9a). In total lysis, the water gradient is less sharp compared to the free shrinkage (Figure 8b), which means the water is better distributed. This is because the tissue permeability is much higher than in the free shrinkage (Figure 9b) at any level of water content.

Natural lysis also shows a better water distribution inside the tissue than in the free shrinkage (Figure 8c). This is due to the formation of the tissue layer that has very high permeability (dark red colored) in the middle of the tissue, which permits water redistribution. This layer appears when the local water activity gets lower than 0.97 (the zero turgid point) in which the permeability suddenly jumps up because of the breakage of the cell membrane (explained in Section 3.1). At the tissue core, the permeability will be lower than in this layer as long as the water activity is still higher than the zero turgid point. In Figure 9, a tissue region with permeability less than 1.1×10^{-15} s is shown in black. The value corresponds to the permeability of a tissue that has a water activity of 0.6 at 25°C, a critical water activity level for safe storage. Note that at a such low water activity (a_w = 0.6), free shrinkage and lysis have a similar tissue permeability. The black region therefore represents a barrier layer for water transport, since the tissue region below this layer has a higher permeability. Figure 9 shows that at average fruit a_w of 0.90 and 0.80, the two lysis cases have a thinner barrier layer than the shrinkage case. If we look back at Figure 7b, the surface water activity of the lysis cases is also higher than the shrinkage case. It means that overall, the barrier layer in the lysis case is not only thinner but also more permeable, which could enhance the drying rate (Figure 7c and d).

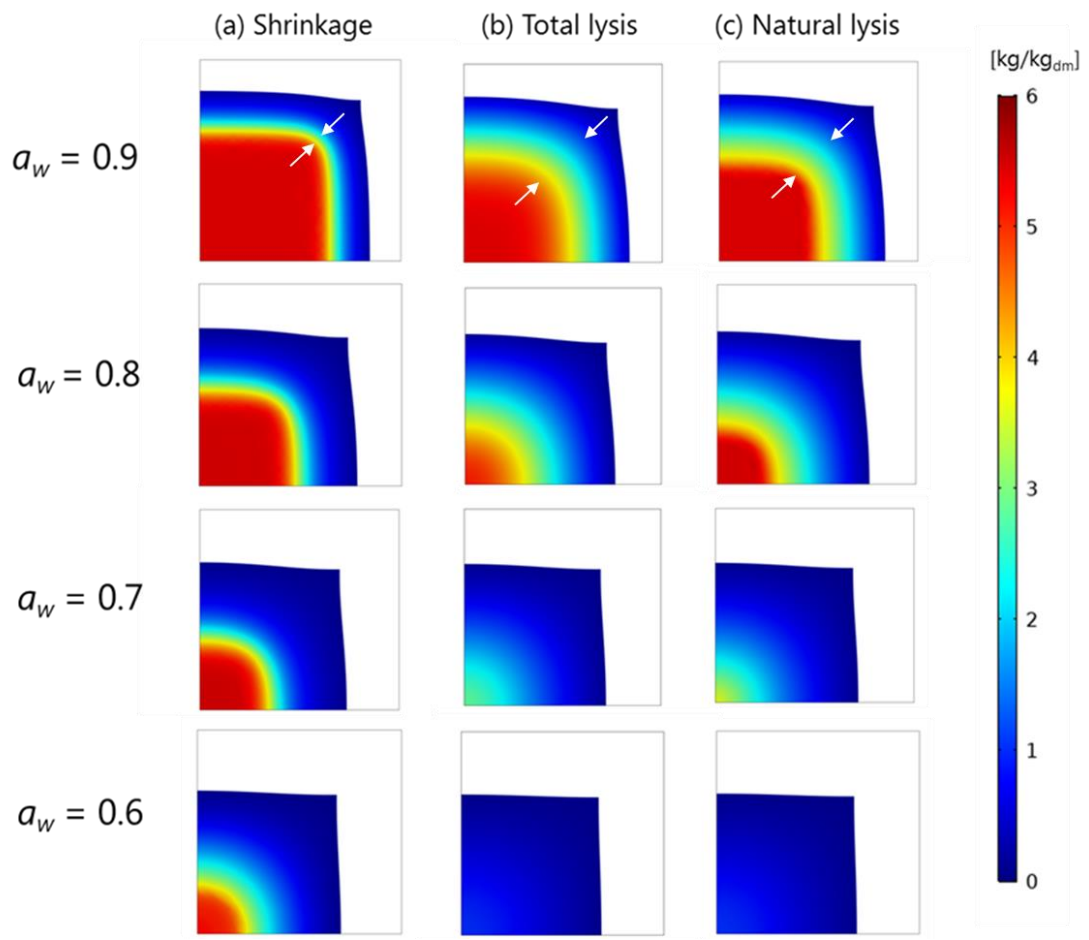

Figure 8. Spatial distribution of water content at a certain level of average water activity over the tissue sample for different scenarios of microstructural changes: free shrinkage, total lysis, natural lysis. The white arrows indicate the part of the tissue where there is a gradient of water content.

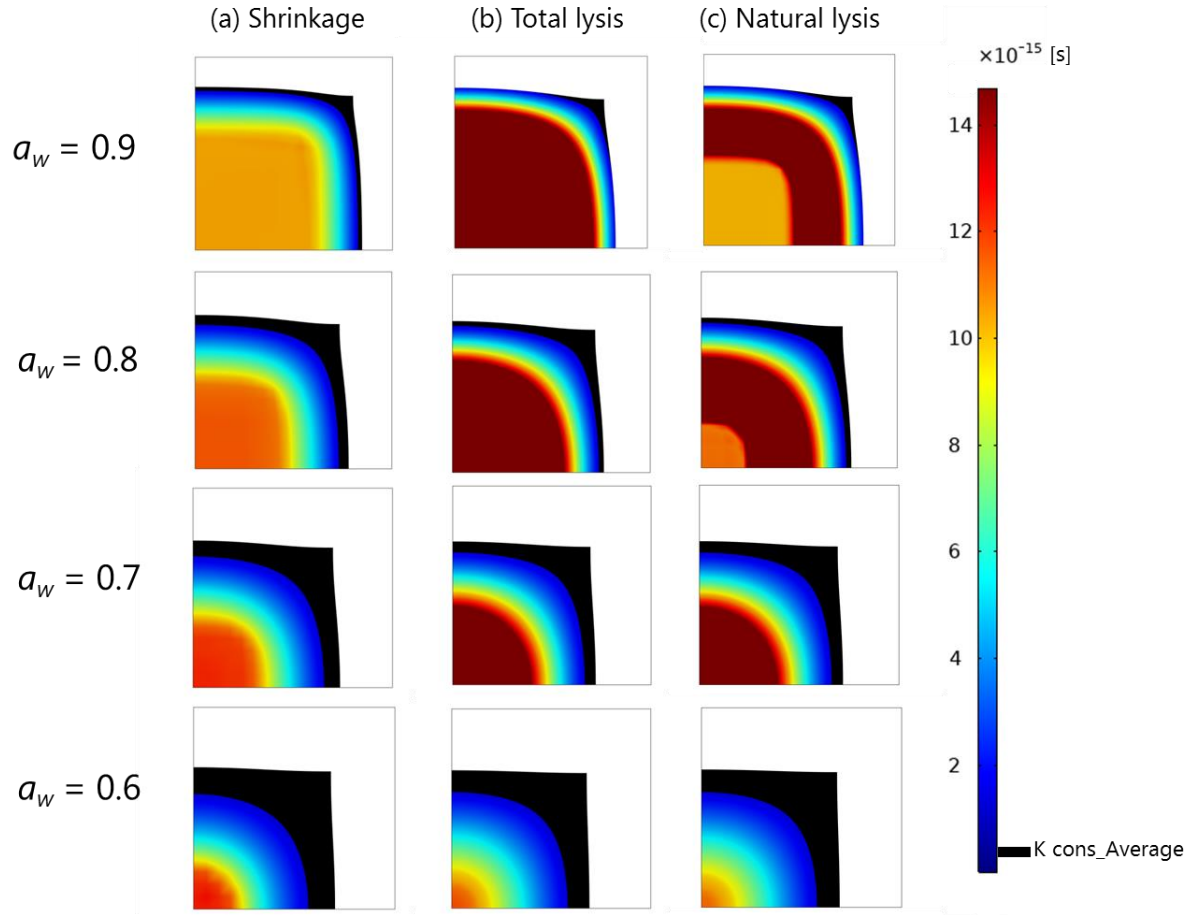

Figure 9. Spatial distribution of effective permeability at a certain average water activity for different scenarios of microstructural changes: free shrinkage, total lysis, natural lysis. The black region is a tissue which has permeability lower than 1.1 x 10^{-15} s.

3.3 Impact of drying kinetics on the microstructural change

With the developed upscaling approach, we can also investigate how the drying rate would eventually affect the microstructural changes in the tissue during drying. For free shrinkage and natural lysis, the drying rates at the different airspeeds and relative humidities are presented in Figure 10. It can be seen that natural lysis causes a higher drying rate than free shrinkage for all drying conditions. Furthermore, the differences between the drying rate of natural lysis and free shrinkage are getting larger either at higher airspeed (up to 100% in 5 m s^{-1} case) or lower air humidity (up to 22 in 10% RH case). This can be explained based on the external and internal resistances of water removal from the tissue. The external resistance is caused by the interaction between material surface and drying air in the form of an air boundary layer (Rodríguez et al. 2018). Higher airspeed results in a smaller boundary layer resistance for water removal at the surface, which is reflected by the increase of CHTC and consequently, CMTC. In the case of low humidity, it is simply increasing the difference in vapor pressure (Equation 26), thus vapor pressure deficit. Tissue with higher permeability, in the case of natural lysis, has a smaller internal resistance to transport water from inside to the surface of the tissue. Therefore, it has a higher drying rate than free shrinkage. This study shows that the benefit of lysis occurrence can be maximized by promoting a higher drying rate, either by increasing the air speed or decreasing the air humidity.

It can also be seen that the impact of airspeed and relative humidity on the drying rate is decreasing at smaller water content. In natural lysis, all cases have almost the same drying rate when the water content drops below 1 kg kg^{-1}. In free shrinkage, it occurs at water content smaller than 2 kg kg^{-1}. This phenomenon happens when the dried tissue is formed at the surface and the surface water activity drops to nearly similar to the air humidity. In this period, the permeability plays the main role in determining the drying rate instead of the external resistance. This is the reason why in natural lysis, the convergence of drying rate happens at a smaller water content than the free shrinkage. At water content of 2 kg kg^{-1} for example, the permeability of natural lysis is still sufficiently high to allow the water to migrate into the surface, which is not the case in free shrinkage. In the following paragraphs, we describe how the drying rate could also inversely impact the microstructural change of the tissue, especially at the beginning of the drying process when the turgid cells in the tissue entering the period of free shrinkage and lysis. Only results from airspeed variations are presented since similar drying behaviors are observed for variations in relative humidity (in smaller extent). For clarity, only a comparison of low drying rate case (at an airspeed of 0.5 m s^{-1}) and high drying rate case (at an airspeed of 5 m s^{-1}) are shown.

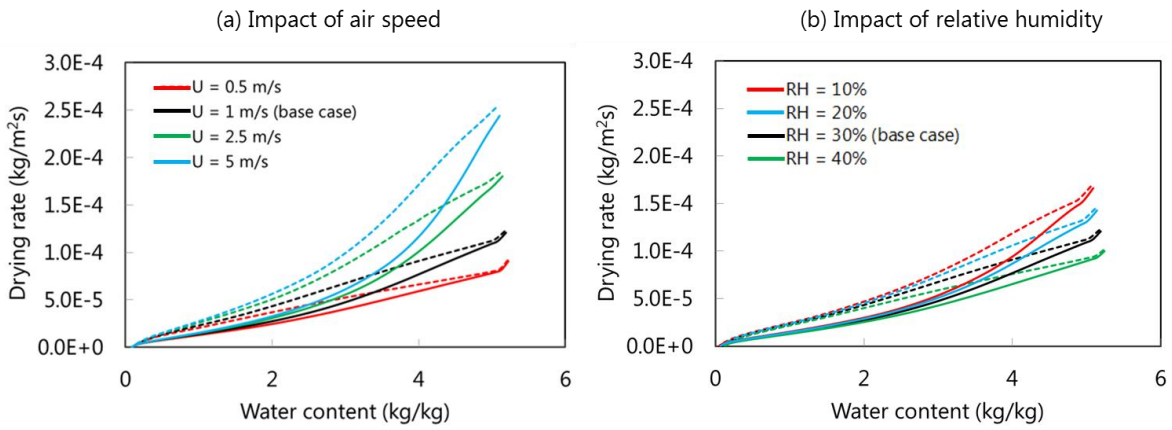

Figure 10. Impact of (a) airspeed and (b) relative humidity on the drying rate of the free shrinkage (solid line) and natural lysis (dashed line) cases.

In Figure 11, we divide the tissue into two regions to show the progress of microstructural changes within the tissue. First is the tissue part where the water activity is higher than 0.97 (in red). Based on our assumption, this region represents the tissue region with turgid cells. The other region has a water activity less than 0.97 (in gray) and represents tissue with shrunken or lysed cells (non-turgid). At the same level of water activity, both free shrinkage and natural lysis show that the turgid region (in red) is always larger in drying at high airspeed (5 m s^{-1}), thus higher drying rate. It means that a higher drying rate causes changes in the microstructure closer to the surface, leaving the tissue below less affected. The progress of microstructural changes for all airspeed variations can be seen in Figure 12a as a volume fraction of the non-turgid tissue. The difference in the progress of microstructural changes between different drying rates can be explained by looking at the permeability profile in Figure 13. In free shrinkage and natural lysis, high airspeed causes steeper gradients in tissue permeability (Figure 13) in the corresponding non-turgid (in gray) region in Figure 12. The resulting barrier layer (black area in Figure 13) is thinner but less permeable, compared to the low airspeed drying. As such, this barrier layer keeps the water

inside the turgid tissue beneath it. The observed phenomena, which are related to changes of permeability with moisture content, could not be unveiled until now. In this study, the upscaling made such insights possible.
At the same airspeed, the main difference between free shrinkage and natural lysis is the formation of a high permeable layer in the natural lysis case (Figure 13b), as also mentioned in Section 3.2. It induces a more uniform moisture content across the tissue at the a certain level of average water activity. Further, it creates a higher volume fraction of the induced microstructural changes compared to free shrinkage case (Figure 12). The cell membrane breakage at the outer surface propagates faster into the tissue interior, compared to the progress of free cell shrinkage. Therefore, at a_w = 0.6, the turgid tissue has been completely changed into a lysed tissue (Figure 11b) while free shrinkage needs to reach a_w of around 0.5 (figure not shown) to change the turgid tissue completely. In lysis case, a fast progression of microstructural changes within the tissue is beneficial, since the membrane breakage increase the permeability of the tissue and subsequently, the overall drying rate.

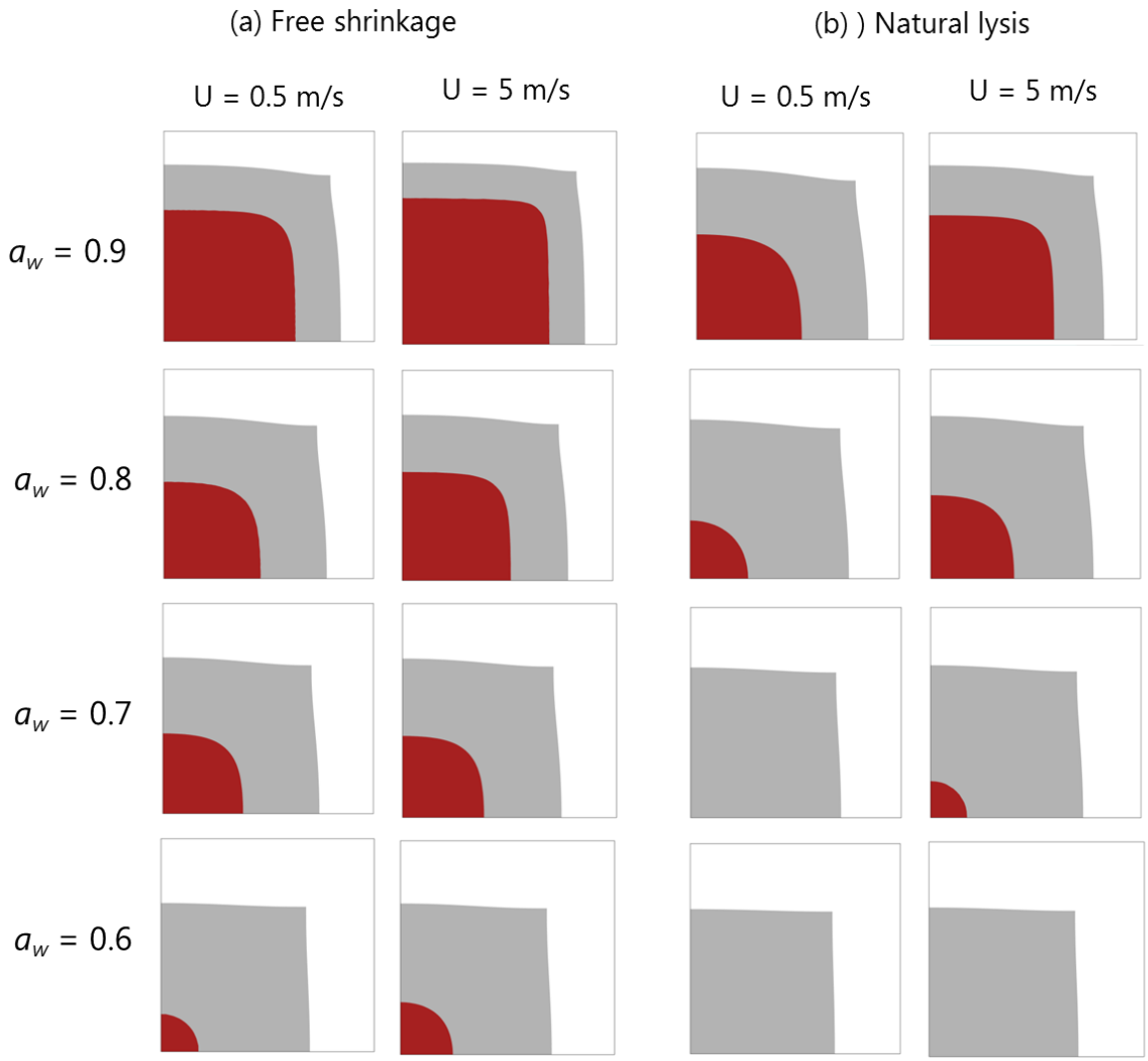

Figure 11. Profile of water activity, showing the tissue region where the cells in the tissue change from the turgid conditions to the free shrinkage or lysis (a_w < 0.97, in gray), and where the cells in the tissue is still turgid (a_w > 0.97, in red) for (a) free shrinkage and (b) natural lysis cases at different drying airspeeds.

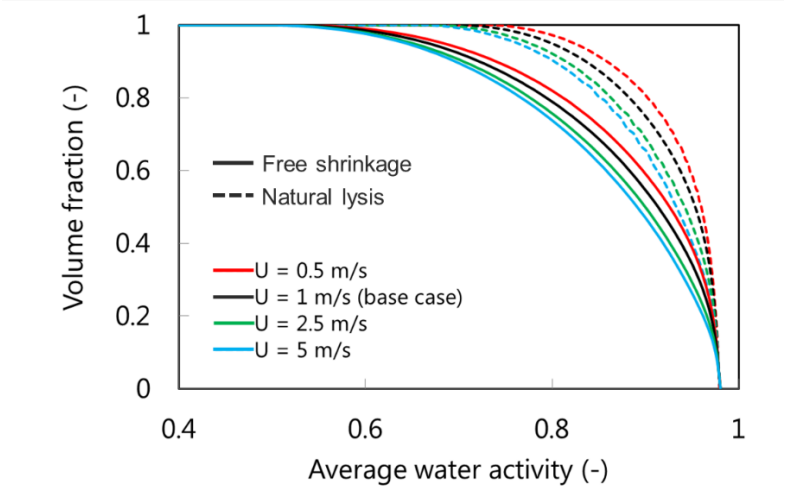

Figure 12. Volume fraction of non-turgid tissue shows the progress of microstructural changes of free shrinkage and natural lysis at different drying airspeed.

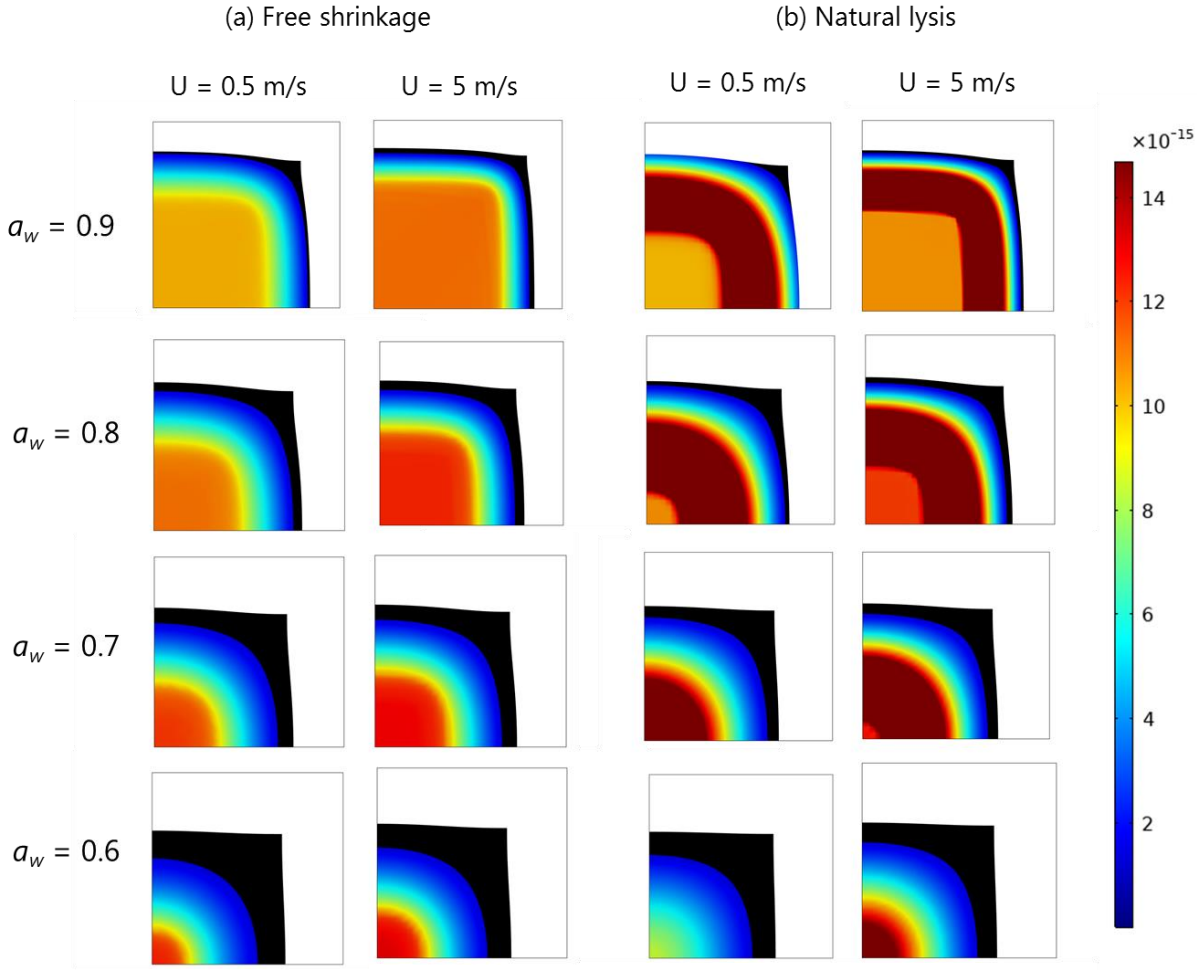

Figure 13. Spatial distribution of effective permeability at a certain level of average water activity for the shrinkage and lysis cases at different drying airspeeds.

3.4 Strategies to reduce drying time

In general, there are two strategies to reduce drying time. The first is to increase the drying rate by modifying the drying conditions (in this case, the airspeed and relative humidity). The second is promoting microstructural changes to enhance water transport within the cellular structure. One possible strategy presented in this study is to stimulate lysis. Lysis can be induced by external processes such as blanching, freeze-thaw cycle (Ando et al. 2016), and electro-permeabilization (Wu et al. 2011; Ade-Omowaye et al. 2002). Our upscaling approach makes quantitative analysis in determining the appropriate drying strategies possible. Assuming a safety limit of water activity at 0.6, the drying times required to reach this value (both as an average for the whole tissue and after the core reaches it) for free shrinkage and total lysis are presented in Table 7. Inducing lysis before drying reduces the drying rate by 26% (from 14 hours to 10.3 hours). It is important to mention that the shrinkage case with the highest airspeed of 5 m s^{-1} gives a slightly longer drying time to achieve average and core water activity of 0.6, than the lysis case with an airspeed of 1 m s^{-1}. Decreasing the relative humidity to 10% also results in a longer drying time than lysis case at 30% RH. It can be seen that increasing airspeed or reducing humidity is not always the best strategy to accelerate the drying process and that inducing lysis is eventually a better option. With such insight, the current study can be extended in future research to analyze the combination of strategies that yields the minimum drying time.

Table 7. Drying time required to achieve average tissue water activity and core water activity of 0.6

Air speed [m s^{-1}]	**Relative humidity [%]**	**Free shrinkage**		**Lysis**	
		Average (0.6)	**Core (0.6)**	**Average (0.6)**	**Core (0.6)**
0.5 m s^{-1}	30	16.6	19.1	12.5	13.8
1 m s^{-1}	30	14	16.7	10.3	11.7
2.5 m s^{-1}	30	11.8	14.7	8.3	9.7
5 m s^{-1}	30	10.7	13.7	7.3	8.6
1 m s^{-1}	10	10.8	14.9	8.7	10.4
1 m s^{-1}	20	12.1	15.7	9.5	11.0
1 m s^{-1}	40	16.5	18.5	11.6	12.8

4 Conclusions

An upscaling approach is developed to study the convective drying process of apple fruit. Compared to the previous mechanistic drying model, the developed approach enables the drying model to include the impact of microstructural changes, a crucial factor that is overlooked in drying modeling. By bridging a microscale and macroscale modeling through the calculation of effective permeability, we identify the need and importance of pretreatment process to modify the microstructure, such as lysis, to optimize the drying process. Simulations suggest that drying leads to a formation of barrier layer at the tissue surface which has a low permeability. This layer can significantly impact the macroscopic drying rate. The permeability of this layer is mainly dependent on the dehydration mechanisms of the cells inside the layer, whether the cells undergo free shrinkage or lysis. The microscale simulation shows that lysis, which can be induced using various pretreatment processes such as blanching, ultrasound and pulse electric field, enhances the tissue permeability up to four times compared to the free shrinkage case. We demonstrate that inducing lysis before drying at an airspeed of 1 m s^{-1} and relative humidity of 30% results in shorter drying time (decreased by 26%) than increasing the airspeed to 5 m s^{-1} or reducing the relative humidity to 10%. This study is not only able to quantify the impact of pretreatment process, but also shows the urgency of bringing a multiscale paradigm in drying modeling of soft cellular material since the macroscopic drying behavior is significantly affected by the microstructural changes.

Acknowledgment

We acknowledge the support of the Swiss National Science Foundation SNSF (project 200021_160047). We thank Dominique Derome for the fruitful discussion during the initial phase of the study. We also thank Bowen Liang at The Ohio State University, for the discussion on the meshing method for the microscale modeling. We acknowledge the support of Stephan Carl at Empa for the X-ray experimental set-up.

Author contributions

T.D. conceptualized the study, wrote the project proposal to secure funding (with input from J.C.), did project administration and was the Principal Investigator (PI) in the project; K.P., T.D., and J.C. developed the methodology; K.P. performed the X-ray experiments and FEm simulations; K.P performed data analysis, interpretation, and visualization of the results; T.D. and J.C. supervised K.P; K.P. wrote the original draft with key inputs from T.D.; T.D. and J.C. critically reviewed and edited the manuscript, and K.P revised the manuscript on the basis of these suggestions.

Reference

Ando, Y. *et al.* (2016) 'Impact of blanching and freeze-thaw pretreatment on drying rate of carrot roots in relation to changes in cell membrane function and cell wall structure', *LWT - Food Science and Technology*. Academic Press, 71, pp. 40–46. doi: 10.1016/J.LWT.2016.03.019.
Aregawi, W. a. *et al.* (2014) 'Prediction of water loss and viscoelastic deformation of apple tissue using a multiscale model.', *Journal of physics: Condensed Matter*, 26(46), p. 464111. doi: 10.1088/0953-8984/26/46/464111.
Aregawi, W. A. *et al.* (2013) 'Modeling of Coupled Water Transport and Large Deformation During Dehydration of Apple Tissue', *Food and Bioprocess Technology*, 6(8), pp. 1963–1978. doi: 10.1007/s11947-012-0862-1.
ASHRAE (2006) 'Chapter 9 - Thermal Properties of Food', in *2006 ASHRAE Handbook - Refrigeration*.
Baldwin, C. A. *et al.* (1996) 'Determination and Characterization of the Structure of a Pore Space from 3D Volume Images', *Journal of Colloid and Interface Science*, 181(1), pp. 79–92. doi: 10.1006/jcis.1996.0358.
Barati, E. and Esfahani, J. A. (2013) 'A novel approach to evaluate the temperature during drying of food products with negligible external resistance to mass transfer', *Journal of Food Engineering*. Elsevier, 114(1), pp. 39–46. doi: 10.1016/J.JFOODENG.2012.07.028.
Bazyma, L. A. *et al.* (2006) 'The investigation of low temperature vacuum drying processes of agricultural materials', *Journal of Food Engineering*. Elsevier, 74(3), pp. 410–415. doi: 10.1016/J.JFOODENG.2005.03.030.
Bellagha, S. *et al.* (2008) 'Desorption isotherms of fresh and osmotically dehydrated apples (Golden delicious)', pp. 45–52.
Ben-Arie, R., Kislev, N. and Frenkel, C. (1979) 'Ultrastructural changes in the cell walls of ripening apple and pear fruit', *Plant Physiology*, 64(2)(2), pp. 197–202. doi: 10.1104/pp.64.2.197.
Bonet, J. and Wood, R. D. (2008) *Nonlinear Continuum Mechanics for Finite Element Analysis, 2nd Edition*. doi: 10.1017/CBO9780511755446.
Caccavale, P., De Bonis, M. V. and Ruocco, G. (2016) 'Conjugate heat and mass transfer in drying: A modeling review', *Journal of Food Engineering*. Elsevier, 176, pp. 28–35. doi: 10.1016/J.JFOODENG.2015.08.031.
Castro, A. M., Mayorga, E. Y. and Moreno, F. L. (2018) 'Mathematical modelling of convective drying of fruits: A review', *Journal of Food Engineering*. Elsevier Ltd, 223, pp. 152–167. doi: 10.1016/j.jfoodeng.2017.12.012.
Castro, A. M., Mayorga, E. Y. and Moreno, F. L. (2019) 'Mathematical modelling of convective drying of feijoa (Acca sellowiana Berg) slices', *Journal of Food Engineering*. Elsevier, 252, pp. 44–52. doi: 10.1016/J.JFOODENG.2019.02.007.
CBI (2008) 'Preserved Fruit and Vegetables: The EU Market for Dried Fruit', *CBI Market Information Database*, pp. 1–22.
Chvoj, Z., Conrad, H. and Cháb, V. (1999) 'Analysis of the Arrhenius shape of adatom diffusion coefficient in a surface model with two energy barriers', *Surface Science*. North-Holland, 442(3), pp. 455–462. doi: 10.1016/S0039-6028(99)00960-7.
Constenla, D. T., Lozano, J. E. and Crapiste, G. H. (1989) 'Thermophysical Properties of Clarified Apple Juice as a Function of Concentration and Temperature', *Journal of Food Science*, 54(3), pp. 663–668. doi: 10.1111/j.1365-2621.1989.tb04677.x.
Coulson, J. . *et al.* (1999) 'Fluid Flow, Heat Transfer and Mass Transfer', in *Chemical Engineering*. Sixth. Elsevier B.V., pp. 381–409.
Defraeye, T. (2017) 'When to stop drying fruit: Insights from hygrothermal modelling', *Applied Thermal Engineering*. Elsevier Ltd, 110, pp. 1128–1136. doi: 10.1016/j.applthermaleng.2016.08.219.
Defraeye, T., Blocken, B. and Carmeliet, J. (2012) 'Analysis of convective heat and mass transfer coefficients for convective drying of a porous flat plate by conjugate modelling', *International Journal of Heat and Mass Transfer*. Elsevier Ltd, 55(1–3), pp. 112–124. doi: 10.1016/j.ijheatmasstransfer.2011.08.047.
Defraeye, T. and Verboven, P. (2016) 'Convective drying of fruit: role and impact of moisture transport properties in modelling', *Journal of Food Engineering*. Elsevier Ltd, 193, pp. 95–107. doi: 10.1016/j.jfoodeng.2016.08.013.
Deng, L.-Z. *et al.* (2017) 'Chemical and physical pretreatments of fruits and vegetables: Effects on drying characteristics and quality attributes – a comprehensive review', *Critical Reviews in Food Science and Nutrition*. Taylor & Francis, 0(0), pp. 1–25. doi: 10.1080/10408398.2017.1409192.
Fanta, S. W. *et al.* (2012) 'Water transport properties of artificial cell walls', *Journal of Food Engineering*. Elsevier Ltd, 108(3), pp. 393–402. doi: 10.1016/j.jfoodeng.2011.09.010.
Fanta, S. W. *et al.* (2013) 'Microscale modeling of water transport in fruit tissue', *Journal of Food Engineering*. Elsevier Ltd, 118(2), pp. 229–237. doi: 10.1016/j.jfoodeng.2013.04.003.
Ferrando, M. and Spiess, W. E. L. (2001) 'Cellular response of plant tissue during the osmotic treatment with sucrose, maltose, and trehalose solutions', *Journal of Food Engineering*, 49(2–3), pp. 115–127. doi: 10.1016/S0260-8774(00)00218-1.

Gulati, T. and Datta, A. K. (2015) 'Mechanistic understanding of case-hardening and texture development during drying of food materials', *Journal of Food Engineering*. Elsevier Ltd, 166, pp. 119–138. doi: 10.1016/j.jfoodeng.2015.05.031.
Herremans, E. *et al.* (2015) 'Automatic analysis of the 3-D microstructure of fruit parenchyma tissue using X-ray micro-CT explains differences in aeration.', *BMC plant biology*. BMC Plant Biology, 15(1), p. 264. doi: 10.1186/s12870-015-0650-y.
Ho, Q. T. *et al.* (2011) 'A Three-Dimensional Multiscale Model for Gas Exchange in Fruit', *Plant Physiology*, 155(3), pp. 1158 LP – 1168. Available at: http://www.plantphysiol.org/content/155/3/1158.abstract.
Ho, Q. T. *et al.* (2013) 'Multiscale modeling in food engineering', *Journal of Food Engineering*. Elsevier Ltd, 114(3), pp. 279–291. doi: 10.1016/j.jfoodeng.2012.08.019.
Holz, M., Heil, Stefan, R. and Sacco, A. (2000) 'Temperature-dependent self-diffusion coefficients of water and six selected molecular liquids for the calibration in acccurate HNMR PFG m', *Phys. Chem. Chem. Phys.*, 2, pp. 4740–4742. doi: 10.1039/b005319h.
Igarashi, T. (1985) 'Heat transfer from a square prism to an air stream', *International Journal of Heat and Mass Transfer*. Pergamon, 28(1), pp. 175–181. doi: 10.1016/0017-9310(85)90019-5.
Janjai, S. *et al.* (2008) 'Finite element simulation of drying of mango', *Biosystems Engineering*. Academic Press, 99(4), pp. 523–531. doi: 10.1016/J.BIOSYSTEMSENG.2007.12.010.
Joardder, M. U. H. *et al.* (2015) 'Effect of Cell Wall Properties on Porosity and Shrinkage of Dried Apple', *International Journal of Food Properties*, 18(10), pp. 2327–2337. doi: 10.1080/10942912.2014.980945.
Kapitz, M. *et al.* (2018) 'Experimental study of the influence of the Prandtl number on the convective heat transfer from a square cylinder', *International Journal of Heat and Mass Transfer*. Pergamon, 120, pp. 471–480. doi: 10.1016/J.IJHEATMASSTRANSFER.2017.12.032.
Karunasena, H. C P *et al.* (2014) 'A coupled SPH-DEM model for micro-scale structural deformations of plant cells during drying', *Applied Mathematical Modelling*, 38(15–16), pp. 3781–3801. doi: 10.1016/j.apm.2013.12.004.
Karunasena, H.C.P. *et al.* (2014) 'A particle based model to simulate microscale morphological changes of plant tissues during drying', *Soft matter*, 10(29), pp. 5249–5268. doi: 10.1039/c4sm00526k.
Karunasena, H. C. P. *et al.* (2015) 'Application of meshfree methods to numerically simulate microscale deformations of different plant food materials during drying', *Journal of Food Engineering*, 146, pp. 209–226. doi: 10.1016/j.jfoodeng.2014.09.011.
Kaya, A., Aydin, O. and Demirtaş, C. (2007) 'Drying Kinetics of Red Delicious Apple', *Biosystems Engineering*, 96(4), pp. 517–524. doi: 10.1016/j.biosystemseng.2006.12.009.
Labuza, T. P. (1972) 'Nutrient losses during drying and storage of dehydrated foods', *C R C Critical Reviews in Food Technology*, 3(2), pp. 217–240. doi: 10.1080/10408397209527139.
Lebovka, N. I., Shynkaryk, N. V. and Vorobiev, E. (2007) 'Pulsed electric field enhanced drying of potato tissue', *Journal of Food Engineering*. doi: 10.1016/j.jfoodeng.2005.10.032.
Lee, D. T. and Schachter, B. J. (1980) 'Two algorithms for constructing a Delaunay triangulation', *International Journal of Computer & Information Sciences*. doi: 10.1007/BF00977785.
Lemus-Mondaca, R. A. *et al.* (2017) 'Modeling 3D conjugate heat and mass transfer for turbulent air drying of Chilean papaya in a direct contact dryer', *Heat and Mass Transfer/Waerme- und Stoffuebertragung*. Springer Berlin Heidelberg, 53(1), pp. 11–24. doi: 10.1007/s00231-016-1799-0.
Léonard, A. *et al.* (2008) 'Moisture Profiles Determination During Convective Drying Using X-Ray Microtomography', *The Canadian Journal of Chemical Engineering*, 83(1), pp. 127–131. doi: 10.1002/cjce.5450830121.
Liu, Z. *et al.* (2016) 'Optimization of pulsed electric field pretreatment parameters for preserving the quality of Raphanus sativus', *Drying Technology*. doi: 10.1080/07373937.2015.1070859.
Maloney, J. O. (2007) *Perrys' Chemical Engineering Handbook*, *Perrys' Chem. Eng. Handb.* doi: 10.1036/0071511245.
Marrero, T. R. and Mason, E. A. (1972) 'Gaseous Diffusion Coefficients', *Journal of Physical and Chemical Reference Data*. doi: 10.1063/1.3253094.
Mebatsion, H. K. *et al.* (2009) 'A novel method for 3-D microstructure modeling of pome fruit tissue using synchrotron radiation tomography images', *Journal of Food Engineering*. Elsevier Ltd, 93(2), pp. 141–148. doi: 10.1016/j.jfoodeng.2009.01.008.
Molz, F. J. (1976) 'Water transport through plant tissue: the apoplasm and symplasm pathways', *Journal of Theoretical Biology*. Academic Press, 59(2), pp. 277–292. doi: 10.1016/0022-5193(76)90170-3.
Moshelion, M., Moran, N. and Chaumont, F. (2004) 'Dynamic changes in the osmotic water permeability of protoplast plasma membrane', *Plant Physiology*, 135(August), pp. 2301–2317. doi: 10.1104/pp.104.043000.1.
Naiqian, W. and Pitts, M. J. (1999) 'Development and validation of a finite element model of an apple fruit cell', *Postharvest Biology and Technology*, 16, pp. 1–8.
Nguyen, T. A. *et al.* (2003) 'An estimation procedure of effective diffusivity in pear tissue by means of a numerical water diffusion model', *Acta Horticulturae*, 599, pp. 541–548. doi: 10.1016/j.jfoodeng.2004.11.019.

Nobel, P. S. (2009) *Physicochemical and environmental plant physiology*. Academic Press. Available at: http://www.sciencedirect.com/science/book/9780123741431 (Accessed: 23 August 2017).
Onwude, D. I. *et al.* (2019) 'Experimental studies and mathematical simulation of intermittent infrared and convective drying of sweet potato (Ipomoea batatas L.)', *Food and Bioproducts Processing*. Elsevier, 114, pp. 163–174. doi: 10.1016/J.FBP.2018.12.006.
Orikasa, T. *et al.* (2018) 'Impact of blanching pretreatment on the drying rate and energy consumption during far-infrared drying of Paprika (Capsicum annuum L.)', *Food Quality and Safety*. doi: 10.1093/fqsafe/fyy006.
Prawiranto, K. *et al.* (2018) 'New insights into the apple fruit dehydration process at the cellular scale by 3D continuum modeling', *Journal of Food Engineering*. Elsevier, 239, pp. 52–63. doi: 10.1016/J.JFOODENG.2018.06.023.
Prawiranto, K. *et al.* (2019) 'Impact of drying methods on the changes of fruit microstructure unveiled by X-ray micro-computed tomography', *RSC Advances*, 9(19), pp. 10606–10624. doi: 10.1039/C9RA00648F.
Rahman, M. M. *et al.* (2016) 'Multi-scale model of food drying: Current status and challenges', *Critical Reviews in Food Science and Nutrition*. Taylor & Francis, 58(5), pp. 1–19. doi: 10.1080/10408398.2016.1227299.
Rodríguez, Ó. *et al.* (2018) 'Application of power ultrasound on the convective drying of fruits and vegetables: effects on quality', *Journal of the Science of Food and Agriculture*, 98(5), pp. 1660–1673. doi: 10.1002/jsfa.8673.
Roman, G. N., Urbicain, M. J. and Rotstein, E. (1982) 'Moisture Equilibrium in Apples at Several Temperatures: Experimental Data and Theoretical Considerations', *Journal of Food Science*, 47(5), pp. 1484–1488. doi: 10.1111/j.1365-2621.1982.tb04966.x.
Schössler, K., Jäger, H. and Knorr, D. (2012) 'Effect of continuous and intermittent ultrasound on drying time and effective diffusivity during convective drying of apple and red bell pepper', *Journal of Food Engineering*. doi: 10.1016/j.jfoodeng.2011.07.018.
Shahari, N. and Hibberd, S. (2014) 'Modelling of drying tropical fruits using multiphase model', *WSEAS Transactions on Mathematics*, 13, pp. 840–851.
Shi, J. and Le Maguer, M. (2002) 'Osmotic Dehydration of Foods: Mass Transfer and Modeling Aspects Osmotic Dehydration of Foods: Mass Transfer and Modeling Aspects', *Food Reviews International*, 9129(November). doi: 10.1081/FRI-120016208.
da Silva, W. P., e Silva, C. M. D. P. S. and Gomes, J. P. (2013) 'Drying description of cylindrical pieces of bananas in different temperatures using diffusion models', *Journal of Food Engineering*. Elsevier, 117(3), pp. 417–424. doi: 10.1016/J.JFOODENG.2013.03.030.
Soysal, Y. *et al.* (2009) 'Intermittent microwave-convective drying of red pepper: Drying kinetics, physical (colour and texture) and sensory quality', *Biosystems Engineering*, 103(4), pp. 455–463. doi: 10.1016/j.biosystemseng.2009.05.010.
Tao, Y. and Sun, D. W. (2015) 'Enhancement of Food Processes by Ultrasound: A Review', *Critical Reviews in Food Science and Nutrition*. doi: 10.1080/10408398.2012.667849.
Tortoe, C., Orchard, J. and Beezer, A. (2008) 'Artificial cell studies in simulated apple and potato starch cell complex during osmotic dehydration', *Journal of Food Quality*, 31(5), pp. 559–570. doi: 10.1111/j.1745-4557.2008.00220.x.
Vega-Galvez, A. *et al.* (2012) 'Effect of temperature and air velocity on drying kinetics, antioxidant capacity, total phenolic content, colour, texture and microstructure of apple (var. Granny Smith) slices', *Food Chemistry*, 132(1), pp. 51–59. doi: 10.1016/j.foodchem.2011.10.029.
Velić, D. *et al.* (2004) 'Influence of airflow velocity on kinetics of convection apple drying', *Journal of Food Engineering*, 64(1), pp. 97–102. doi: 10.1016/j.jfoodeng.2003.09.016.
Wang, C. X., Wang, L. and Thomas, C. R. (2004) 'Modelling the mechanical properties of single suspension-cultured tomato cells', *Annals of Botany*, 93(4), pp. 443–453. doi: 10.1093/aob/mch062.
Wijerathne, W. D. C. C. *et al.* (2019) 'A coarse-grained multiscale model to simulate morphological changes of food-plant tissues undergoing drying', *Soft Matter*. doi: 10.1039/c8sm01593g.
Yamaki, S. (1984) 'Isolation of vacuoles from immature apple fruit flesh and compartmentation of sugars, organic acids, phenolic compounds and amino acids', *Plant and Cell Physiology*, 25(1), pp. 151–166.
Yoshida, H. *et al.* (2014) 'Application of Brief Hot Water Soaking as a Pre-treatment in Kiwifruit Drying', *Nippon Shokuhin Kagaku Kogaku Kaishi*. doi: 10.3136/nskkk.61.151.
Zlatanović, I., Komatina, M. and Antonijević, D. (2013) 'Low-temperature convective drying of apple cubes', *Applied Thermal Engineering*, 53(1), pp. 114–123. doi: 10.1016/j.applthermaleng.2013.01.012.

Supplementary material A

Calculating the effective permeability K_{eff} in different REV size.

The largest sample used had an edge length of 3 mm and consisted of 1051 cells. A smaller sample with an edge length of 2 mm was extracted from the center of the 3 mm sample, and so on until samples with an edge length of 1 mm and 0.5 mm were also obtained (Figure A). A thick cell wall was generated due to the limited resolution of the X-ray micro-CT (voxel size = 8.5 µm). Image erosion and subsequent geometrical algorithms presented in Section 2.1.1 only worked for voxel erosion of more than three voxels. Hence, the resulting cell wall thickness was around 25 µm. For apple tissue, the cell wall thickness is in the range of 1 to 10 µm (Ben-Arie et al. 1979; Mebatsion et al. 2009; Joardder et al. 2015). As the main purpose of this REV analysis was to compare the permeability of different sample sizes, the realistic cell wall thickness was not required. The microstructural components of the samples were presented in Table 4. Steady-state simulation of water transport was done in each of the REVs, by setting up the water activity at 0.98 (turgid condition), so no deformation. The comparison of microstructural components and the calculated effective permeability are presented in Table 4.

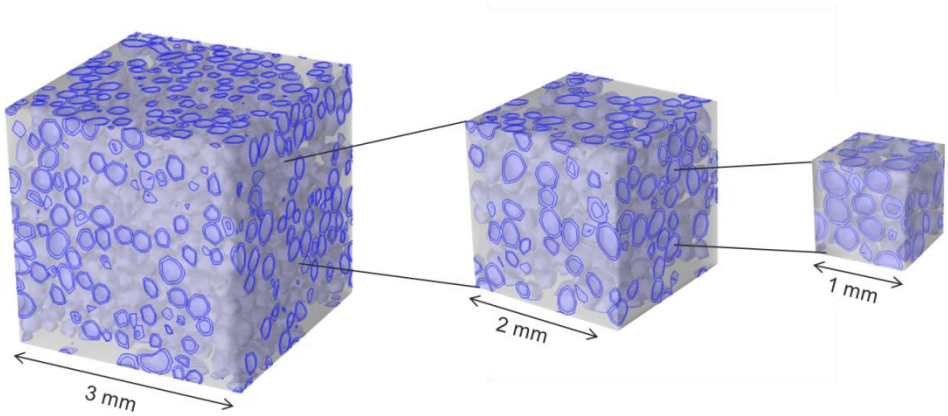

Figure A. Tissue sample used for determining the Representative Elementary Volume (REV). A cubical tissue with an edge length of 3 mm was divided into smaller tissue (2 mm, 1 mm and 0.5 mm). The protoplast and cell wall domains are highlighted in blue.

Supplementary material B

Comparison between experiments and simulations with a multiscale approach

Results of the macroscale modeling using the upscaled moisture transport properties are compared with experimental data of (T. Defraeye and Verboven 2016) to check the reliability and accuracy of the upscaling approach. The free shrinkage case shows a good agreement in terms of the water content, especially during the first 10 hours of drying, although the drying rate was a bit higher (Figure B a and b). The lysis case, however, overpredicts the drying rate that gives a relatively fast moisture removal at the first 7 hours. These differences can be understood since the experimental procedure of (T. Defraeye and Verboven 2016) did not include any steps to promotes lysis. The cells may undergo lysis naturally at some point during drying, but the analysis of the occurrence was not the focus of the experiment. The tissue temperature decreases due to the evaporative cooling effect as the water is removed from the tissue surface. The two simulation cases exhibit a lower core temperature during the first 10 hours of drying compared to the experimental data. The differences are in the range of 1 – 2 °C. The faster drying rate induces larger effect of evaporative cooling. In the simulations, the core temperature reaches the wet-bulb temperature of 14.75°C. It is the minimum temperature that can be attained at the given drying conditions (T = 23°C and RH = 40%).

In general, some discrepancies are found between the experimental data and simulation results. They can be explained by two reasons. Firstly, the moisture transport properties of the sample in the experiment are not the same as the upscaled properties used in macroscale modeling. Biological variabilities exist between individual fruit due to the type of cultivar, ripeness level, cultivation sites or harvest year, etc. In the context of microscale modeling, the biological variability results in differences in porosity, cell size, cell wall thickness, membrane permeability, among others. These could affect the calculated upscaled properties. Secondly, the discrepancies may come from the unmodeled physics at a later stage of drying. As it is shown in other studies (Karathanos, Kanellopoulos, and Belessiotis 1996b; Madiouli et al. 2012), porous layers are formed during drying as a result of cell wall stiffening due to moisture removal. In this case, the moisture transfer mechanism changes from a liquid diffusion-dominated mechanism through the cell wall to vapor diffusion-dominated mechanism through the pores. Furthermore, the decreasing shrinkage rate at this drying stage makes the moisture path to reach the tissue surface longer. This phenomenon is not captured by the microscale model and it will overpredict the effective permeability of the tissue. As a result, the drying rate is higher in the simulation especially between three until seven hours of drying. Nevertheless, the macroscale modeling using the upscaled properties gives adequate matches with the experimental data where the drying rates and temperature are still in the same order of magnitude.

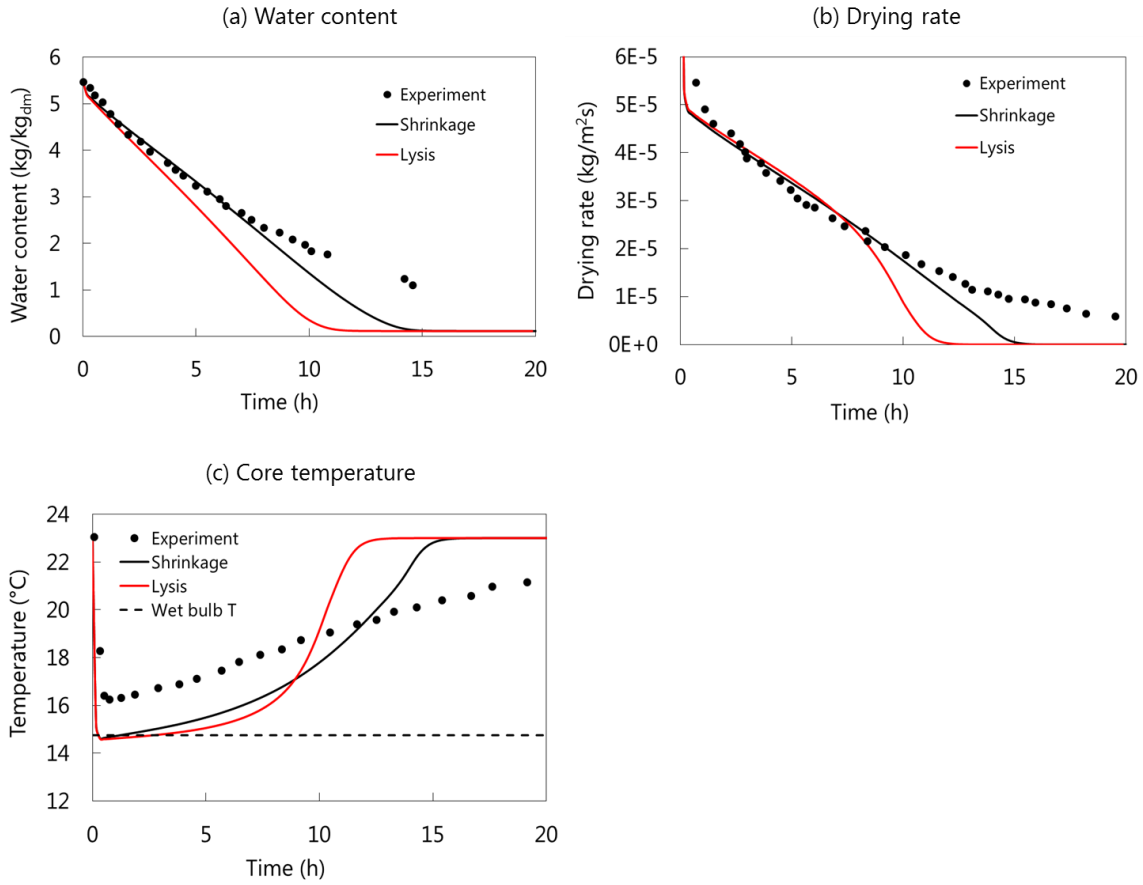

Figure B. Comparison between the macroscale simulation and experimental results of (Defraeye and Verboven, 2016): (a) water content, (b) drying rate and (c) core temperature. Two dehydration cases are considered in the simulations, namely free shrinkage and total lysis.